

Simulating the effect of fabric bending stiffness on the wrinkling behaviour of biaxial fabrics during preforming

F. Yu, S. Chen, L.T. Harper*, N.A. Warrior

Composites Research Group, University of Nottingham, Nottingham, UK

Corresponding author: L. T. Harper

E-mail address: (lee.harper@nottingham.ac.uk)

Abstract

A macroscopic finite element model has been established to investigate the forming-induced wrinkling behaviour for bi-axial fabrics. Results indicate that using a linear bending model with a constant bending stiffness produces unrealistic wrinkle patterns in the fabric plies. A non-linear bending model produces more accurate forming induced wrinkle patterns compared to experimental data, since the bending stiffness parameter is varied as a function of the applied forming load to account for the onset of fibre buckling. Areas of high in-plane shear are more likely to induce out-of-plane wrinkles, indicating a positive correlation between wrinkling onset and shear deformation. A new methodology has been developed to quantitatively evaluate the severity of fabric wrinkles based on the FE simulation results. The distance between the surface of the preform and the mould tool is used to locate areas with out-of-plane defects, using the principal curvature to isolate wrinkles from areas of fabric bridging (poor conformity).

Keywords

A. Fabrics/Textiles; B. Defects; C. Finite element analysis (FEA); E. Forming.

1 Introduction

Fabric preforming processes for liquid composite moulding have been widely used to facilitate high-volume production, but manufacturing-induced defects such as wrinkles can significantly compromise the mechanical performance of the final components. Numerical process simulations have been used to reduce the cost of design-for-manufacture [1-3], by predicting the location and severity of manufacturing defects rather than using experimental trial and error approaches. Furthermore, the change in fibre orientation due to the forming process can be predicted and used to facilitate downstream modelling of the resin infusion process and to determine the structural performance of the final component.

Kinematic drape simulation codes [4] use a purely geometrical approach to compute fabric drape patterns, with no consideration for mechanical material properties or process conditions. Finite Element (FE) simulations enable the physics of the forming problem to be modelled and therefore consider the influence of process parameters, including contacts and friction between the components. Consequently, they can be used for more detailed analyses to indicate the likelihood of defects, such as fabric wrinkling, bridging and ply splitting.

It is common for FE forming simulations to use a membrane approach to model the fabric plies [5, 6], to minimise the number of degrees of freedom and reduce the computation time. Membrane elements can be used to take into account the in-plane shear behaviour between the primary yarns and have successfully been used to predict yarn orientation [7] and material draw-in during forming. Macroscale wrinkles can be identified from the shear angle distribution by locating areas that have exceeded the “locking angle” [8]. This is a computationally efficient method but it is only a qualitative approach for detecting defects, as it is unable to characterise the true size and shape of wrinkles [9, 10]. Subsequently, a number of studies [9-13] have indicated the importance of incorporating the effects of fabric bending for predicting more realistic wrinkle patterns.

Fabric bending stiffness is typically measured to be much lower than the axial stiffness in the fibre directions, due to fibre sliding [10] and yarn buckling [13]. Consequently, it is not possible to use standard shell elements in commercial finite element software, in which the bending stiffness is calculated from the axial moduli using shell theory. Hybrid membrane and beam/shell meshes [11, 12, 14], bespoke semi-discrete shell elements [9] and laminate layup approaches [13, 15] have been proposed to decouple the fabric bending behaviour from the axial moduli, due to this weak relationship. It is worth noting that it is this weak relationship that facilitates the forming of these materials, enabling large curvatures to be generated in the fabric ply without damaging the fibres.

The standard cantilever test [16] is the most commonly used method to characterise the bending behaviour of composite fabrics [17], producing a constant bending stiffness value that can be implemented in FE forming simulations [14, 18]. However, non-linear bending behaviour has been observed for a wide range of engineering fabrics [12, 13, 19, 20] and alternative test methods have been explored [12, 17]. The authors previously characterised the non-linear bending behaviour of a biaxial non-crimp fabric (NCF) using a revised cantilever test, employing a Structured White Light Scanner (SWLS) to obtain an accurate representation of the deflected specimen shape. A polynomial function was used to fit the side profile shape to obtain the non-linear bending moment as a function of curvature along the specimen. This approach was used to provide input data for a new macroscale FE material model, using a laminated shell-element approach to account for the non-linear effects of fibre-orientation dependent bending. It was reported that using a linear bending model (LBM) under-predicted the tip deflection in a simple cantilever fabric bending test, with an average relative error of 17% compared to experimental data [13]. The response using a non-linear bending model (NLBM) was more representative, with an average relative error of just 0.6%. Further simulations of a bias extension test demonstrated that the predicted wrinkle amplitude of the fabric sample was comparable to experimental data, with a root mean square error of less than 2.5%.

The work presented in the current paper implements this laminated shell-element approach for fabric forming simulations, to investigate the significance of using a NLBM to capture the material bending

behaviour, compared to a simpler LBM with constant bending stiffness. The model is applied to two different fabrics; a balanced twill weave with a relatively low bending stiffness and a non-crimp fabric with asymmetric in-plane shear behaviour with a higher bending stiffness. A hemisphere forming rig is used to generate experimental data to validate the model, with a gap between the blank holder and die to create controlled wrinkle patterns.

Comparing wrinkle patterns between simulation and experimental data for complex geometries can be problematic and is generally qualitative. Whilst the shape and location of out-of-plane wrinkles can be approximated by incorporating the effects of the fabric bending stiffness [9, 12, 21], detailed evaluation relies on observations from the deformed FE mesh. The distance deviation between the deformed fabric ply and the baseline tool surface provides a quantitative measure for the amplitude of wrinkles [13, 22-24], but this is unable to assess the severity of individual wrinkles since the surface curvature is overlooked [25]. To quantitatively measure wrinkling behaviour, Dörr et al. [26] calculated the nodal curvature for the deformed fabric by taking a weighted average of the angular differences between the normals of elements sharing a common node. However, the curvature obtained was dependent on the local mesh discretisation and was unable to accurately measure the radius of the local ply waviness, since the curvature was calculated in an average manner.

In the current work, wrinkle patterns determined from the deformed FE mesh have been compared to point cloud datasets determined by SWLS. Based on Abaqus/Python scripting, surface defects have been located by evaluating the conformity between the deformed fabric mesh and the baseline surface. Principal curvatures, i.e. eigenvalues of the shape operator at each point, have been calculated using an iterative quadric fitting method [27], enabling an effective measure for the waviness radius along the critical direction of wrinkle defects.

2 Experimental Approach

2.1 Materials

Two carbon fibre fabric reinforcements were used in this study; a NCF from Hexcel (FCIM359) and a balanced twill-weave fabric from Carr Reinforcements Ltd (38616). Material parameters for both fabrics are listed in Table 1. Picture frame shear testing was conducted to determine the shear resistance of the woven fabric, using the methodology outlined by Harrison et al. [28]. The normalised shear force versus shear angle curve was fitted using a 7th order polynomial function, as presented in Table 1. The shear resistance for the NCF was previously determined by the authors in an earlier study [8].

2.2 Bending behaviour characterisation

The bending behaviour for both fabrics was determined using two different methods to investigate the suitability of the NLBM for predicting out-of-plane wrinkles. Firstly, the standard cantilever method was used to produce a constant value for the bending stiffness, according to BS EN ISO 9073-7; 1998 [16]. Secondly, a revised cantilever method was used to define a non-linear relationship between the bending stiffness and the degree of specimen curvature, as previously outlined by Yu et al. [13]. A SWLS (model HP Pro S3) was used to obtain accurate 3D representations of the deformed fabric specimens when using this revised method. The scan data was used to fit a polynomial to the deflection curve taken from the side profile of the specimen. A single loading configuration was used to establish the curvature and bending moment as functions of curvilinear coordinates along the specimen. The NCF specimens were tested at two different orientations, with either the 0° or 90° fibres on the uppermost surface to account for the specimen asymmetry. The woven fabric was tested in the warp direction only, as this material was balanced in both directions. Voce's model [29] was used to fit the experimental data to obtain an explicit function for the bending moment versus curvature relationship to be used in the numerical simulation.

As shown in Figure 1 and Figure 2, the bending stiffness decreases with an increase in curvature for each material. Overall, the bending stiffness for the NCF is significantly higher than the woven material over the range of curvature values presented (note difference in magnitude of y-axes between Figure 1(b) and Figure 2(b)). However, the bending stiffness for the NCF specimens decreases more rapidly with respect to curvature compared to the woven material, which can be attributed to tow buckling as previously discussed by Yu et al. [13]. The dashed straight lines in Figure 1 and Figure 2 denote constant bending stiffness values. $B_{41.5}$ was measured at a fixed deflection angle of 41.5° using the standard cantilever test [16]. $B_{41.5}^{wov}$ was measured to be 0.00022 Nm, but different bending stiffnesses were measured for the NCF in the positive and negative bending configurations, i.e. $B_{41.5}^{NCF,pos} = 0.0038$ Nm and $B_{41.5}^{NCF,neg} = 0.0032$ Nm respectively, due to the fabric asymmetry. The value B_{init} represents the stiffness at zero curvature and the asymptote value B_{inf} represents the stiffness at large curvatures, which were both derived from the revised non-linear cantilever test data [13]. All bending stiffness values are presented in Table 1 for both materials. According to the studies conducted by Yu et al. [13], the NLBM produces more realistic predictions for the fabric response during bending when compared against experimental data, as applying a simple LBM underestimates the deflection considerably.

2.3 Press tool forming

Press tool forming trials were conducted for both fabrics using a hemisphere rig developed at the University of Nottingham. Two forming configurations were considered, as shown in Table 2. For Case A, a controlled 7 mm gap was introduced between the blank holder and die to enable the fabric blank to wrinkle out-of-plane in a controlled manner during the stroke of the punch. For Case B, a clamping force of 1000 N was applied to the closed blank holder (no gap) to control the material draw-in during forming, preventing the fabric blank from excessively wrinkling. A single fabric ply was used for Case A and two plies of the same fibre orientation were used for Case B, for both fabric types. The warp yarn direction of the woven fabric (0/90) and the stitch direction of the NCF were initially aligned with

the edge of the blank holder prior to forming, as shown in Table 2. A constant punch velocity of 100 mm/min was used at ambient temperature. The stroke length was 50mm, measured from the initial point of contact with the upper surface of the fabric blank. A small amount (6%wt) of reactive binder (Momentive Epikote 620) was evenly distributed on the upper surface of each ply prior to forming. The powder binder was activated by cartridge heaters embedded in the blank holders and the punch once the final stroke had been reached. The temperature was subsequently ramped up to 165 °C and held for 10 minutes to cure the binder in order to keep the shape of the produced preform.

2.4 Wrinkle Measurements

The shapes of the deformed hemisphere specimens were captured using the SWLS. Ambersil Flaw Detector was uniformly sprayed onto the deformed fabric specimens once removed from the forming tool, to eliminate excessive reflection from the carbon fibres. The prepared specimens were positioned on a turntable connected to the scanner to take a series of scans at different angles, to capture full 3D representations of each preform. Open-source software, CloudCompare [30], was used to determine the wrinkle amplitude of the preforms produced by forming Case B, by comparing the point cloud of the deformed specimen against the punch geometry and the bottom blank holder. As shown in Figure 6, the repeatability associated with the SWLS measurements for forming Case A was found to be high, with a root mean square error (RMSE) of less than 3% for the woven fabric and less than 8% for the NCF.

3 Simulation Approach

3.1 Material modelling

A previously developed modelling approach [13] was employed to implement the bending behaviour of the two fabrics into a simulation framework via a user defined material subroutine (VUMAT) in Abaqus/Explicit. The fabric bending stiffness was decoupled from its in-plane stiffness using the

Abaqus built-in laminate shell layup (i.e. Composite Layup Toolset), where each fabric ply was represented by three artificial layers as shown in Figure 3. The curvature of each yarn was calculated based on the gradient of the strains at the integration points through the shell thickness. A single integration point was assigned to the central layer to remove any contribution to the overall bending stiffness of the shell element. A single integration point was also assigned to each surface layer for this study, in order to minimise the computation time [13], since the stress-strain relationship was assumed to be elastic.

The moduli of the three layers within the layup were updated during the analysis to replicate the bending moment versus curvature relationship derived from the experiments. The bending stiffness of each yarn was defined based on the current fibre orientation frame, by adding the bending contribution of each primary yarn to an established non-orthogonal constitutive model [7, 8, 31, 32]. This enables the bending stiffness to be updated as the fabric undergoes in-plane shear. The actual density and thickness values were assigned to the shell elements for each fabric, as presented in Table 1. The implementation of the VUMAT material model is presented in more detail in Appendix A.

3.2 Wrinkle evaluation

All forms of macroscale defect, including wrinkling, bridging and fabric folding, exhibit a deviation in the distance measured from the tool surface to the formed fabric part. Therefore, this nodal deviation can be used to locate the position of surface defects and measure the amplitude. As shown in Figure 4, the nodal distance d_p measured from Node P on the deformed mesh of the fabric ply to Point P' on the tool surface is:

$$d_p = \|\overrightarrow{PP'}\| = \|\overrightarrow{OP} - \overrightarrow{OP'}\| \quad (1)$$

where Point O is the origin of the coordinate system and Node P' on the tool surface is the closest point to Node P on the fabric mesh.

In practice, a local sub-region of the tool mesh was determined to reduce the computation time (region enclosed by red lines in Figure 4). Nodes on the tool mesh in the vicinity of Node P were determined using a bounding sphere, using built-in Python functions within Abaqus. The radius of the bounding sphere was adjusted to ensure that the sub-region comprised at least nine elements. The location of P' was subsequently determined by searching for the closest point on the tool surface to Node P within the sub-region, where Point P' does not necessarily coincide with the nodes on the tool mesh.

As shown in Figure 5, out-of-plane defects were detected if the nodal distance d_p exceeded a critical value d_p^{crit} , the distance from the mid-plane of each fabric ply to the tool surface. For example, d_p^{crit} is equal to half of the ply thickness if a single-ply preform is used. Elements on the fabric mesh that contain nodal distances greater than this threshold are considered to exhibit at least one form of out-of-plane defect, i.e. bridging or wrinkling. The surface curvature was subsequently calculated for these elements to isolate fabric wrinkles (Zone A in Figure 5) from fabric bridging (i.e. poor conformity, denoted by Zone B in Figure 5). Zone C in Figure 5 indicates curved regions that correctly match features on the surface of the tool where no defects were detected. The maximum absolute value of the principal curvatures was employed to determine the wrinkle radius:

$$\kappa_p^{\text{max}} = \text{Max}(|\kappa_{1,p}|, |\kappa_{2,p}|) \quad (2)$$

where, $\kappa_{1,p}$ and $\kappa_{2,p}$ are the first and second principal curvatures for node P , respectively.

Since a smooth surface geometry can be locally approximated using a quadratic polynomial surface, an iterative quadric fitting technique was used to determine the nodal curvatures over the fabric ply [27]. This method has previously been validated [33] for accurately computing curvatures for unstructured meshes with complex geometric features. The procedure was implemented using Abaqus/Python scripting, as described in Appendix B.

The distance between the fabric and the tool surface, d_p^{crit} was initially used to identify regions containing out-of-plane defects, but local changes in the distribution of κ_p^{max} were used to isolate regions containing out-of-plane wrinkles. Areas of bridging on the hemisphere tool are straightforward to identify, as they are typically found around the equator of the dome (see $R = 6\text{mm}$ in Table 2), but this method becomes more relevant as the complexity of the formed shape increases.

3.3 Model setup

For Case A, the laminate shell element approach (using S4R elements) was compared to a membrane element approach [8] (using quadrilateral membrane elements M4DR) to demonstrate the significance of incorporating the bending stiffness term into the simulation for predicting realistic fabric wrinkle patterns. The element edge length was 2 mm for both fabrics. The polynomials representing the in-plane shear compliance for each material are presented in Table 1. All parts of the tooling, including the hemispherical punch and the blank holders, were modelled as rigid bodies. Interactions at all interfaces were modelled using a penalty contact algorithm, assuming an isotropic Coulomb-based friction model. The tool-fabric and fabric-fabric friction coefficients were measured to be 0.23 and 0.36 respectively [8]. A vertical displacement of 50 mm was applied to the punch. The axial fibre modulus was assigned to be 3.0 GPa in each case to limit the axial strain in the fibre direction to less than 1%, as recommended by Harrison et al. [18]. Both linear and non-linear bending relations were implemented using the laminated shell element approach, to evaluate the sensitivity of the predicted wrinkle patterns to the bending stiffness input. The run time for the shell element approach was approximately 16 hours for the NLBM and 12 hours for the LBM, using a step time of 3 seconds. In comparison, the run time for the membrane element-based approach was 2.5 hours for the same step size. (The computer specification was the same for both cases: Intel Xeon CPU E5-1620 v3 @ 3.50GHz).

For Case B, only the NLBM was used to simulate the bending behaviour of the fabrics, and the element edge size was assigned to be 1 mm to capture small wrinkles. The blank holder was subjected to a

clamping force of 1000N, which was applied as a uniform pressure over the surface area. The time increment for the explicit analysis was set to be 3E-6 s, with the total time step extended to 30 s to avoid excessive inertial effects. The total run time for Case B was therefore longer than Case A (26 hours) using the same computer specification. All other model parameters remained the same.

4 Results and discussion

4.1 Forming Case A: Wrinkle pattern identification

4.1.1 Woven fabric

Simulation results for the woven fabric are compared against the experimental data in Figure 7 for a range of scenarios using the laminated shell element model for forming Case A. An output from the membrane element model is also included for comparison, which overlooks the influence of fabric bending. The wrinkle pattern for the experimental specimen in Figure 7(a) is broadly symmetric about the x and y axes, since the shear behaviour of this woven fabric is symmetrical in the positive and negative shear directions. Wrinkles lie along the diagonal directions of the ply where the fabric undergoes large shear deformation (see the magnified view of the sheared fabric yarns in Figure 7(a)). There are no apparent wrinkles in the dome area where the fabric contacts the hemispherical punch. The wrinkle amplitude presented in Figure 7(b) was simulated using the membrane element model. Due to the lack of constraint from the blank holder (i.e. 7mm gap), each membrane element was unable to carry the bending load. Consequently, elements distorted locally until reaching a balanced status, leading to irregular wrinkle patterns in the fabric ply. Previous forming simulation studies have indicated that areas of high in-plane shear correlate well to areas of wrinkling [8, 34-37]. However in the current study, the membrane element approach is unable to deliver a stable analysis for the fabric forming process because the blank is not suitably constrained between the blank holders, causing unrealistic out-of-plane deformation. The bending behaviour therefore seems to dominate the wrinkling behaviour.

Figure 7 (c) shows the simulated results for the laminated shell element approach using the NLBM. One primary wrinkle is predicted in each quadrant, which is in good agreement with the experimental scan data. Figure 7(d) to Figure 7(f) show the predicted wrinkle patterns using the laminated shell element approach with a linear bending model (LBM), assuming a range of constant bending rigidities taken from the experimental data in Figure 1, i.e. B_{init}^{wov} , $B_{41.5^\circ}^{wov}$ and B_{inf}^{wov} . Generally, the number of predicted wrinkles decreases as the bending stiffness increases. Whilst the experimental stiffness values are easier to measure and the LBM is simpler to implement, none of these simulations produce realistic wrinkle patterns compared to the experimental data.

To provide further clarity, the cross-sectional shapes of the simulated wrinkles from Sections A-A' and B-B' (see Figure 7(a)) have been compared against the experimental data in Figure 8. For Section A-A' (see Figure 8(a)) both the LBM and NLBM are in reasonable agreement with the experimental curve. The RMSE for the LBM using the $B_{41.5^\circ}^{wov}$ bending stiffness value is 8.3 %, compared with 6.4% for the NLBM. For Section B-B' (see Figure 8(b)), additional wrinkles are predicted by the LBM ($B_{41.5^\circ}^{wov}$) compared to the experimental data, since the bending stiffness is assumed to be constant. This curve (LBM $B_{41.5^\circ}^{wov}$) represents the solution if the bending stiffness is determined using the standard cantilever test. In comparison, the wrinkle amplitude predicted by the NLBM is consistent with the experimental curve, with a RMSE of 1.1%. This demonstrates the importance of incorporating the non-linear bending response of the fabric into the forming simulation for this lightweight woven material, which generally exhibits a low bending stiffness.

The root mean square of the bending moments along the warp and weft yarns, M_f^{RMS} , is plotted in Figure 9(a), with the maximum value found in areas where the fabric ply passes through the edge of the hole of the blank holder. In Figure 9(b), the probability of M_f^{RMS} shows that the bending moment obtained using the LBM is much higher than that predicted by the NLBM. This indicates that the linear model, which is dependent on the constant stiffness value derived by the standard cantilever test, is likely to overestimate the internal bending moment of the fabric.

4.1.2 Non-crimp fabric

Simulation results for the NCF are compared against experimental data in Figure 10. Results from the membrane element approach are not presented here because similar irregular wrinkle patterns in the fabric ply were observed as for the woven material above, therefore only results from the laminate shell approach have been included. The same material models (LBM and NLBM) have been considered as for the woven material, to investigate the suitability of the LBM for higher bending stiffness materials.

Three primary wrinkles can be observed in both the positive and negative sheared areas of the NCF ply from the experimental data in Figure 10(a). The negative shear induced wrinkles (top and bottom of the hemisphere in the y-direction) are wider and longer than wrinkles resulting from the positive shear region (left and right of the hemisphere in the x-direction), which indicates the influence of the asymmetric shear resistance on the wrinkling behaviour.

The wrinkling pattern predicted by the NLBM (see Figure 10(b)) agrees well with the experimental data, indicating the suitability of the NLBM for simulating the wrinkling behaviour of the NCF. Figure 10(c) to Figure 10(e) present the wrinkle patterns predicted using constant bending stiffnesses in the LBM, i.e. B_{init}^{NCF} , $B_{41.5^\circ}^{NCF}$ and B_{inf}^{NCF} respectively. As the bending stiffness input parameter increases, the number of individual wrinkles decreases and the general size of each wrinkle increases, as previously observed for the woven material.

The predicted formed shape using the initial bending stiffness B_{init}^{NCF} with the LBM exhibits a similar wrinkle pattern to the NLBM prediction, but this model is unable to capture some of the features along the wrinkle edges where significant fabric bending occurs. This is because these regions experience higher levels of curvature and therefore tow buckling is likely to occur, which is not captured by the LBM. However, the NLBM requires more computational effort compared to the LBM (16 hours compared to 12 hours), so further refinement of the LBM may be worthwhile for approximating the

wrinkle pattern for fabrics with high initial bending stiffness. According to a previous study [13], B_{init} can be approximated successfully using the standard cantilever test [16] using a low angular deflection.

Wrinkle amplitudes taken through Sections A-A' and B-B' (see Figure 10(a) for positions) were compared against experimental data from 3 repeat hemispheres, as shown in Figure 11. The grey areas correspond to the range of wrinkle amplitudes determined from the three experimental repeats. In the positive shear region (Section A-A'), the wrinkle amplitude predicted by the NLBM captures the shape of the experimental measurements, but the wrinkle area is wider than the experimental data. The wrinkle amplitude predicted by the NLBM is generally within the error band of the experimental data in the negative shear region (Section B-B'). These sectioned views demonstrate that the NLBM is more reliable for predicting the wrinkle patterns than either of the two LBMs shown ($B_{41.5^\circ}^{NCF}$ or B_{inf}^{NCF}).

Figure 12 shows how the simulated wrinkle patterns develop as the punch displacement increases from 30 mm to 50 mm, according to the shear angle θ_{shr} and the nodal distance d_p . At a punch displacement of 30 mm, areas of the fabric experiencing high in-plane shear (both positive and negative) undergo out-of-plane deformation (see Figure 12(a)). This indicates a positive correlation between areas of high in-plane shear and out-of-plane deformation for the NCF, potentially leading to out-of-plane wrinkles. The wrinkled fabrics in areas of positive shear undergo further buckling at a punch displacement of 40 mm, since the bending stiffness decreases with increasing curvature, resulting in more wrinkles to accommodate the material draw-in (see Figure 12(b)). Results at different displacements therefore indicate that wrinkle initiation is caused by excessive shear deformation, but wrinkle propagation is dominated by the fabric bending stiffness as it changes with increasing curvature and in-plane shear.

Figure 13(a) shows the distribution of the bending moment M_f^{RMS} for both the linear and non-linear bending models (where $B_{41.5^\circ}^{NCF}$ is used as the input for the LBM, since it is the commonly derived bending stiffness from the standard cantilevered bending test). The NLBM predicts significantly lower levels of bending moment for the NCF material compared to the LBM, as previously observed for the

woven fabric. A summary of the bending moment in the warp direction is presented in Figure 13(b), which shows that the probability of M_f^{RMS} predicted by the NLBM is lower than the curve for the LBM. Using a constant bending stiffness for the LBM produced higher bending moments, since the bending stiffness does not vary with the bending deformation to account for fibre buckling, leading to large unrealistic areas of wrinkling over the ply surface.

4.2 Forming Case B: Isolation of defect type

The wrinkle evaluation method presented in Section 3.2 was used to identify forming induced defects for Case B, using only simulation results produced by the NLBM.

The distribution of defects according to the nodal deviation d_p and curvature κ_p^{max} for the woven fabric are plotted in Figure 14, using the nodal coordinates from the deformed fabric mesh. Only the curved region of the hemisphere preform is of interest for this study, since the blank holder prevents any out-of-plane defects in the flat region. There is clearance between the punch and the hole in the blank holder, since the hemisphere rig uses a punch and die arrangement, rather than matched male and female tools. The deformed fabric mesh therefore correctly exhibits a distance deviation from the tool surface of approximately 1mm around the equator of the hemisphere as expected (see Figure 14(a)). However, there is no apparent change in the distribution of surface curvature κ_p^{max} in this region (see Figure 14(b)), indicating that no wrinkles are present. This agrees with the SWLS images of the formed samples presented in Figure 14(c).

Figure 15(a) presents the deformed shape of the experimental NCF specimen scanned from both the concave and convex sides, since only one fibre orientation is visible from each side. Numerous wrinkles are observed in the positive shear regions highlighted in red in Figure 15(a), which correlate well with the simulated wrinkle pattern in Figure 15(b). The longitudinal orientation of the wrinkles in the scanned images follow the same direction as the stitches on the hemisphere. The stitches in these regions are subjected to tensile strain, influencing the out-of-plane wrinkle pattern.

Figure 15(c) shows plots of the nodal deviation d_p for the mid-plane of the topmost ply on the convex side to the forming tool reference surface. Similar to the prediction for the woven fabric, an area of bridging is found around the base of the hemisphere. The predicted maximum amplitude is 2.6 mm in this region, but the average amplitude is similar to the woven material case at approximately 1.0 mm. By plotting the surface curvature, κ_p^{\max} in Figure 15(d), wrinkling defects are isolated from the regions of fabric bridging. The distribution of κ_p^{\max} also generally follows the longitudinal direction of the macroscale wrinkles, with the critical areas highlighted in red ($0.5 \text{ mm}^{-1} < \kappa_p^{\max} < 1.5 \text{ mm}^{-1}$) found in the positive shear region. These correspond to a wrinkle radius of 0.7 – 2.0 mm.

Figure 15(e) presents the axial fibre strain, ε_{f1} , along one of the primary yarn directions. Wrinkles observed along the boundary of the positive and negative shear regions are induced by compressive strains along the primary yarns, as indicated by the negative values for ε_{f1} . These compression induced wrinkles are also observed in the same locations in the experimental scan data (Figure 15(a)), with yarn buckling typically observed on each side of the NCF ply. The macroscale FE simulation captures the main wrinkling characteristics, but it cannot precisely replicate detailed features that occur due to the mesoscale architecture, such as the influence of the stitch direction and the discrete yarn orientations on each side of the NCF ply.

5 Conclusions

Experiments and numerical simulations were performed to investigate the forming induced wrinkling behaviour for two bi-axial fabrics, a balanced twill weave fabric and a pillar-stitched NCF. Controlled wrinkle patterns were generated by introducing a gap between the blank holder and die during experimental hemisphere forming tests. Symmetrical wrinkle patterns were observed when forming the balanced woven fabric, whereas wrinkles exhibited different shapes in regions of positive and negative shear for the NCF, due to the asymmetric shear resistance caused by the through-thickness pillar stitching. This indicates the dependency of the wrinkling behaviour on the mesoscale architecture of the fabric.

Due to the absence of bending resistance, simulations using membrane elements were unable to produce realistic deformed shapes when the fabric ply was poorly constrained out of plane with the open blank holder. This indicates the importance of accounting for the fabric bending stiffness when explicitly modelling the wrinkling behaviour of fabrics during complex forming scenarios.

A linear bending model (LBM) was employed for fabric forming simulations using a laminate shell element approach, indicating that a constant bending stiffness measured from the standard cantilever test may overestimate the internal bending moment along the fibre directions, leading to large unrealistic areas of wrinkling over the ply surface. In contrast, employing a non-linear bending model (NLBM) with a locally variable bending stiffness produced more realistic predictions for the formed shape containing large macroscale wrinkles, regardless of the fabric stiffness or mesoscale fibre architecture. Analyses on the local surface deviation and the internal bending moment indicate that the evolution of fabric bending with increasing punch displacement dominates the propagation of wrinkles during the forming simulation, with areas subjected to high in-plane shear more likely to experience out-of-plane wrinkles.

A strategy was developed to quantitatively visualise the severity of macroscale defects by post-processing the simulation results. The nodal distance between the fabric and tool was shown to be a logical way to locate surface defects. The maximum principal curvature was identified as a suitable measure to determine the radius of preform wrinkles enabling them to be isolated from areas of fabric bridging. Results show that the distribution of the maximum value of the principal curvatures coincides with the longitudinal direction of wrinkles. This macroscale FE continuum approach captures the main wrinkling characteristics for the NCF material, but it is difficult to precisely replicate detailed features that are an artefact of the mesoscale architecture, such as the influence of the stitch direction and the discrete yarn orientations on each side of the NCF ply.

6 Acknowledgement

This work was funded by the Engineering and Physical Sciences Research Council, as part of the “EPSRC Future Composites Manufacturing Research Hub” (EP/P006701/1). The authors would also like to acknowledge funding from the China Scholarship Council (CSC) and the Aviation Industry Corporation of China (AVIC).

Appendix A Fabric model and implementation

According to previous work by the authors [13], when assigning a single integration point to each layer within the laminate shell element, the bending stiffness parallel to the fibres, B_{fi} (where $i = 1, 2$ denotes the two fibre directions), can be written as

$$B_{fi} = \frac{1}{16} E_{fi}^{surf} (h - t^{core})(h + t^{core})^2 \quad (\text{A. 1})$$

where E_{fi}^{surf} is the Young's modulus assigned to the top and bottom surface layers, h is the thickness of the element and t^{core} is the thickness of the central layer. The nominal Young's modulus of each fabric ply along the i^{th} yarn (i.e. E_{fi}^{ply}) is determined according to the Rule of Mixtures:

$$E_{fi}^{ply} = E_{fi}^{surf} \left(\frac{h - t^{core}}{h} \right) + E_{fi}^{core} \left(\frac{t^{core}}{h} \right) \quad (\text{A. 2})$$

where E_{fi}^{core} is the Young's modulus of the central layer.

In practice, E_{fi}^{ply} and B_{fi} , are input parameters, which are used to determine the moduli of each ply within the layup.

An established non-orthogonal constitutive model [7, 31, 32, 34] was employed to track the in-plane fibre direction during forming, enabling the bending contribution of each yarn to be taken into consideration in order to update the fabric bending behaviour according to the in-plane shear deformation. In Abaqus/Explicit, the strain increment is supplied in the Green-Naghdi (GN) frame at each integration point. The base vectors of the GN frame in the initial configuration, ${}^0\mathbf{g}_\alpha$ ($\alpha = 1, 2, 3$),

can be updated using the rotation tensor \mathbf{R} obtained from the polar decomposition of the deformation gradient \mathbf{F}

$$\mathbf{R} = \mathbf{F}\mathbf{U}^{-1} \quad (\text{A. 3})$$

$$\mathbf{g}_\alpha = \mathbf{R} \cdot {}^0\mathbf{g}_\alpha \quad (\text{A. 4})$$

where \mathbf{U} is the right stretch tensor. Let ${}^0\mathbf{e}_{fi}$ denote the initial fibre directions, where the current fibre directions, \mathbf{e}_{fi} , are traced using deformation gradient, \mathbf{F} ,

$$\mathbf{e}_{fi} = \frac{\mathbf{F} \cdot {}^0\mathbf{e}_{fi}}{\|\mathbf{F} \cdot {}^0\mathbf{e}_{fi}\|} \quad (\text{A. 5})$$

The corresponding contravariant vectors of \mathbf{e}_{fi} are

$$\mathbf{e}^{fi} = \frac{\mathbf{e}_{fi} - (\mathbf{e}_{fi} \cdot \mathbf{e}_{fj}) \cdot \mathbf{e}_{fj}}{\|\mathbf{e}_{fi} - (\mathbf{e}_{fi} \cdot \mathbf{e}_{fj}) \cdot \mathbf{e}_{fj}\|}, i \neq j \quad (\text{A. 6})$$

The normal vectors of the fabric surface are determined as

$$\mathbf{e}_{f3} = \mathbf{e}^{f3} = \frac{\mathbf{e}_{f1} \times \mathbf{e}^{f2}}{\|\mathbf{e}_{f1} \times \mathbf{e}^{f2}\|} = \frac{\mathbf{e}^{f1} \times \mathbf{e}_{f2}}{\|\mathbf{e}^{f1} \times \mathbf{e}_{f2}\|} \quad (\text{A. 7})$$

Consequently, the current fibre coordinate frames corresponding to \mathbf{e}_{f1} and \mathbf{e}_{f2} are established based on two sets of base vectors, i.e. $[\mathbf{e}_{f1}, \mathbf{e}^{f2}, \mathbf{e}^{f3}]$ and $[\mathbf{e}^{f1}, \mathbf{e}_{f2}, \mathbf{e}^{f3}]$ respectively. The transformation matrices between the GN frame and the fibre frames are

$$\mathbf{Q}_{f1} = \mathbf{Q}_{f1 \rightarrow GN} = \begin{bmatrix} \mathbf{g}_1 \cdot \mathbf{e}_{f1} & \mathbf{g}_1 \cdot \mathbf{e}^{f2} & \mathbf{g}_1 \cdot \mathbf{e}^{f3} \\ \mathbf{g}_2 \cdot \mathbf{e}_{f1} & \mathbf{g}_2 \cdot \mathbf{e}^{f2} & \mathbf{g}_2 \cdot \mathbf{e}^{f3} \\ \mathbf{g}_3 \cdot \mathbf{e}_{f1} & \mathbf{g}_3 \cdot \mathbf{e}^{f2} & \mathbf{g}_3 \cdot \mathbf{e}^{f3} \end{bmatrix} \quad (\text{A. 8})$$

$$\mathbf{Q}_{f2} = \mathbf{Q}_{f2 \rightarrow GN} = \begin{bmatrix} \mathbf{g}_1 \cdot \mathbf{e}^{f1} & \mathbf{g}_1 \cdot \mathbf{e}_{f2} & \mathbf{g}_1 \cdot \mathbf{e}^{f3} \\ \mathbf{g}_2 \cdot \mathbf{e}^{f1} & \mathbf{g}_2 \cdot \mathbf{e}_{f2} & \mathbf{g}_2 \cdot \mathbf{e}^{f3} \\ \mathbf{g}_3 \cdot \mathbf{e}^{f1} & \mathbf{g}_3 \cdot \mathbf{e}_{f2} & \mathbf{g}_3 \cdot \mathbf{e}^{f3} \end{bmatrix} \quad (\text{A. 9})$$

The strain increment in the GN frame, $d\boldsymbol{\varepsilon}_{GN}$ can be transformed to the fibre frames

$$d\boldsymbol{\varepsilon}_{fi} = \mathbf{Q}_{fi}^T \cdot d\boldsymbol{\varepsilon}_{GN} \cdot \mathbf{Q}_{fi} \quad (\text{A. 10})$$

Thus, stress increments in the fibre frames can be computed using the corresponding strain increments

$$d\boldsymbol{\sigma}_{fi} = \mathbf{C}_{fi} : d\boldsymbol{\varepsilon}_{fi} \quad (\text{A. 11})$$

where \mathbf{C}_{fi} is the constitutive tensor in the i^{th} fibre direction. The explicit forms of Eq. (A. 11) can be determined for the two fibres by assuming the elastic moduli in the fibre directions and the shear modulus are the only non-zero values:

$$\begin{bmatrix} d\sigma_{11} \\ d\sigma_{22} \\ d\sigma_{12} \end{bmatrix}_{f1} = \begin{bmatrix} E_{f1}^* & 0 & 0 \\ 0 & 0 & 0 \\ 0 & 0 & G_{12}(\gamma) \end{bmatrix} \begin{bmatrix} d\varepsilon_{11} \\ d\varepsilon_{22} \\ d\varepsilon_{12} \end{bmatrix}_{f1} \quad (\text{A. 12})$$

$$\begin{bmatrix} d\sigma_{11} \\ d\sigma_{22} \\ d\sigma_{12} \end{bmatrix}_{f2} = \begin{bmatrix} 0 & 0 & 0 \\ 0 & E_{f2}^* & 0 \\ 0 & 0 & G_{12}(\gamma) \end{bmatrix} \begin{bmatrix} d\varepsilon_{11} \\ d\varepsilon_{22} \\ d\varepsilon_{12} \end{bmatrix}_{f2} \quad (\text{A. 13})$$

where, γ is the shear angle ($\gamma = 2\varepsilon_{12}$), and the subscript '**' denotes the through-thickness location of the integration point in the laminate shell element. If the integration point is in the central layer then $E_{fi}^* = E_{fi}^{\text{core}}$, otherwise $E_{fi}^* = E_{fi}^{\text{surf}}$. It is assumed that the contribution from each yarn to the fabric shear force is equal [31], therefore $G_{12}(\gamma)$ can be determined from the normalised shear force (F_{norm}) in Table 1:

$$G_{12}(\gamma) = \frac{F_{\text{norm}}(\gamma)}{h} \quad (\text{A. 14})$$

The stress tensor in each fibre frame at the end of the time increment, $\boldsymbol{\sigma}_{fi}^{\text{new}}$, is computed by adding the stress increment tensor to the stress tensor at the beginning of this time increment $\boldsymbol{\sigma}_{fi}^{\text{old}}$

$$\boldsymbol{\sigma}_{fi}^{\text{new}} = \boldsymbol{\sigma}_{fi}^{\text{old}} + d\boldsymbol{\sigma}_{fi} \quad (\text{A. 15})$$

Finally, the stress tensor in the fibre frames are transformed back to the GN frame and superimposed for updating the stress tensor at the integration point:

$$\boldsymbol{\sigma}_{GN}^{\text{new}} = \mathbf{Q}_{f1} \cdot \boldsymbol{\sigma}_{f1}^{\text{new}} \cdot \mathbf{Q}_{f1}^T + \mathbf{Q}_{f2} \cdot \boldsymbol{\sigma}_{f2}^{\text{new}} \cdot \mathbf{Q}_{f2}^T \quad (\text{A. 16})$$

According to the Koiter-Sanders shell theory [37], the fibre strain, $\boldsymbol{\varepsilon}_{fi}$, in the fibre frames can be expressed by the fibre strain on the shell reference surface, $\bar{\boldsymbol{\varepsilon}}_{fi}$, and the fibre curvature, κ_{fi} :

$$\boldsymbol{\varepsilon}_{fi} = \bar{\boldsymbol{\varepsilon}}_{fi} + \bar{F}_{33} z_0 \kappa_{fi} \quad (\text{A. 17})$$

where, z_0 is the initial distance from the integration point to the midplane of the shell element. The thickness change \bar{F}_{33} can be derived from the in-plane components of the deformation gradient F_{ij} ($i, j = 1, 2$), i.e.

$$\bar{F}_{33} = \frac{1}{F_{11}F_{22} - F_{12}F_{21}} \quad (\text{A. 18})$$

The procedure for updating the bending moment and curvature is shown in Figure A. 1. During each time increment, the non-orthogonal constitutive framework is employed to determine the strain along each fibre direction. Eq. (A. 17) is then used to calculate the current curvature of each yarn, which relates to the bending stiffness. The calculation of the bending moment and curvature in each of the fibre frames requires data from adjacent integration points in the thickness direction, which is not directly available in the VUMAT. Therefore, a user defined subroutine VEXTERNALDB is employed to access an external database for passing updated element information between time increments.

Appendix B Implementation of the iterative quadric fitting for nodal curvature estimation

According to the method presented in Ref. [27], the mesh assembled by a series of finite elements can be locally approximated using a quadric polynomial surface at each node of interest. As shown in Figure 4, the nodal normal \mathbf{n}_P defines a local tangent plane of a quadric surface fitted by the nodes within the neighbourhood of the node P . By assuming that the quadric surface passes through the node P , a quadric polynomial of the following form is employed to perform data fitting

$$z = ax^2 + bxy + cy^2 + dx + ey \quad (\text{B. 1})$$

where $(x, y, z)^T$ are the coordinates at the local coordinate system, with the origin at the node P . The nodal curvature at P can be determined according to the following steps:

1. Find elements sharing the node P , and split each quadrilateral element into triangles as shown in Figure 4.
2. Estimates the nodal normal at P by taking a weighted average over the normal vectors of triangle facets sharing the node P . The nodal normal, \mathbf{n}_P is calculated as follows:

$$\mathbf{n}_P = \sum_{i=1}^N \frac{\overrightarrow{PP_i} \times \overrightarrow{PP_{i+1}}}{\|\overrightarrow{PP_i}\|^2 \cdot \|\overrightarrow{PP_{i+1}}\|^2} \quad (\text{B. 2})$$

where N is the number of triangle facets around the node P . P_i and P_{i+1} are nodes of the i^{th} triangle facet arranged in a counter-clockwise order. The plane defined by the normal \mathbf{n}_P is therefore the tangent plane of the quadric surface at the node P .

3. A local coordinate system $\{\mathbf{e}_1, \mathbf{e}_2, \mathbf{e}_3\}$ is established on the tangent plane of the node P to perform quadric fitting, where \mathbf{e}_3 is aligned with the nodal normal \mathbf{n}_P . The basis vector \mathbf{e}_1 can be determined by projecting the first basis vector of the global coordinate system $\{\mathbf{E}_1, \mathbf{E}_2, \mathbf{E}_3\}$ onto the tangent plane

$$\mathbf{e}_1 = \frac{\mathbf{E}_1 - (\mathbf{E}_1 \cdot \mathbf{e}_3)\mathbf{e}_3}{\|\mathbf{E}_1 - (\mathbf{E}_1 \cdot \mathbf{e}_3)\mathbf{e}_3\|} \quad (\text{B. 3})$$

\mathbf{e}_2 can be determined by taking the cross product of \mathbf{e}_3 and \mathbf{e}_1

$$\mathbf{e}_2 = \frac{\mathbf{e}_3 \times \mathbf{e}_1}{\|\mathbf{e}_3 \times \mathbf{e}_1\|} \quad (\text{B. 4})$$

In practice, if \mathbf{n}_P is parallel to \mathbf{E}_1 then the projection of \mathbf{E}_2 on the tangent plane can be used to form the local frame.

4. Select the nodes of the elements sharing the node P for quadric fitting, as shown in Figure 4. The coordinates of the selected nodes expressed in the global coordinate system need to be mapped to the local coordinate system. Let \mathbf{X}_G be the coordinates of a node expressed in the global coordinate system, then the coordinates of that node in the local coordinate system are expressed as

$$\mathbf{x} = \mathbf{R}(\mathbf{X}_G - \mathbf{X}_P) \quad (\text{B. 5})$$

where \mathbf{X}_P denotes the coordinates of the node P expressed in the global coordinate system. \mathbf{R} is the transformation matrix, which takes the following form

$$\mathbf{R} = \begin{bmatrix} \mathbf{e}_1 \cdot \mathbf{E}_1 & \mathbf{e}_1 \cdot \mathbf{E}_2 & \mathbf{e}_1 \cdot \mathbf{E}_3 \\ \mathbf{e}_2 \cdot \mathbf{E}_1 & \mathbf{e}_2 \cdot \mathbf{E}_2 & \mathbf{e}_2 \cdot \mathbf{E}_3 \\ \mathbf{e}_3 \cdot \mathbf{E}_1 & \mathbf{e}_3 \cdot \mathbf{E}_2 & \mathbf{e}_3 \cdot \mathbf{E}_3 \end{bmatrix} \quad (\text{B. 6})$$

5. The coefficients in Eq. (B. 1) are obtained by solving the linear least squares fitting problem

$$\begin{bmatrix} x_1^2 & x_1 y_1 & y_1^2 & x_1 & y_1 \\ \vdots & \vdots & \vdots & \vdots & \vdots \\ x_N^2 & x_N y_N & y_N^2 & x_N & y_N \end{bmatrix} \begin{bmatrix} a \\ b \\ c \\ d \\ e \end{bmatrix} = \begin{bmatrix} z_1 \\ \vdots \\ z_N \end{bmatrix} \quad (\text{B. 7})$$

6. Estimate the new nodal normal at P using

$$\mathbf{n}_P^{\text{new}} = \frac{[-d, -e, 1]^T}{\sqrt{d^2 + e^2 + 1}} \quad (\text{B. 8})$$

Consequently, the nodal coordinates can be mapped to a new local coordinate system by assigning the normal \mathbf{e}_3 in Step 2 to be $\mathbf{R}^T \mathbf{n}_P^{\text{new}}$. The procedure from Step 2 to Step 6 is repeated until the incremental change in the nodal normal falls below a defined tolerance.

7. Estimate the surface curvatures as follow

$$K_P = \frac{4ac - b^2}{(1 + d^2 + e^2)^2}$$

$$H_P = \frac{a + c + ae^2 + cd^2 - bde}{(1 + d^2 + e^2)^{3/2}} \quad (\text{B. 9})$$

$$\kappa_{1,2} = H_P \pm \sqrt{H_P^2 - K_P}$$

where $K_P = \kappa_1 \kappa_2$, which is the Gauss curvature. $H_P = \frac{1}{2}(\kappa_1 + \kappa_2)$ is the mean curvature at the node P . $\kappa_{1,2}$ is the first and second principal curvatures.

References

- [1] Chen, S., O.P.L. McGregor, A. Endruweit, M.T. Elsmore, D.S.A. De Focatiis, L.T. Harper, and N.A. Warrior, *Double diaphragm forming simulation for complex composite structures*. Composites Part A: Applied Science and Manufacturing, 2017. **95**: p. 346-358 DOI: 10.1016/j.compositesa.2017.01.017.
- [2] Boisse, P., N. Hamila, and A. Madeo, *Modelling the development of defects during composite reinforcements and prepreg forming*. Philos Trans A Math Phys Eng Sci, 2016. **374**(2071): p. 20150269 DOI: 10.1098/rsta.2015.0269.
- [3] Thompson, A., J.P.-H. Belnoue, and S.R. Hallett. *Numerical modelling of defect generation during preforming of multiple layers of 2D woven fabrics*. in *Proceedings of ECCM17 conference, Munich, Germany*. 2016.
- [4] Hancock, S.G. and K.D. Potter, *The use of kinematic drape modelling to inform the hand lay-up of complex composite components using woven reinforcements*. Composites Part A: Applied Science and Manufacturing, 2006. **37**(3): p. 413-422 DOI: <https://doi.org/10.1016/j.compositesa.2005.05.044>.

- [5] Peng, X. and F. Ding, *Validation of a non-orthogonal constitutive model for woven composite fabrics via hemispherical stamping simulation*. Composites Part A: Applied Science and Manufacturing, 2011. **42**(4): p. 400-407 DOI: 10.1016/j.compositesa.2010.12.014.
- [6] Yu, W.-R., P. Harrison, and A. Long, *Finite element forming simulation for non-crimp fabrics using a non-orthogonal constitutive equation*. Composites Part A: Applied Science and Manufacturing, 2005. **36**(8): p. 1079-1093 DOI: 10.1016/j.compositesa.2005.01.007.
- [7] Khan, M.A., T. Mabrouki, E. Vidal-Sallé, and P. Boisse, *Numerical and experimental analyses of woven composite reinforcement forming using a hypoelastic behaviour. Application to the double dome benchmark*. Journal of Materials Processing Technology, 2010. **210**(2): p. 378-388 DOI: 10.1016/j.jmatprotec.2009.09.027.
- [8] Chen, S., O.P.L. McGregor, L.T. Harper, A. Endruweit, and N.A. Warrior, *Defect formation during preforming of a bi-axial non-crimp fabric with a pillar stitch pattern*. Composites Part A: Applied Science and Manufacturing, 2016. **91**: p. 156-167 DOI: 10.1016/j.compositesa.2016.09.016.
- [9] Boisse, P., N. Hamila, E. Vidal-Sallé, and F. Dumont, *Simulation of wrinkling during textile composite reinforcement forming. Influence of tensile, in-plane shear and bending stiffnesses*. Composites Science and Technology, 2011. **71**(5): p. 683-692 DOI: 10.1016/j.compscitech.2011.01.011.
- [10] Liang, B., N. Hamila, M. Peillon, and P. Boisse, *Analysis of thermoplastic prepreg bending stiffness during manufacturing and of its influence on wrinkling simulations*. Composites Part A: Applied Science and Manufacturing, 2014. **67**: p. 111-122 DOI: 10.1016/j.compositesa.2014.08.020.
- [11] Harrison, P., *Modelling the forming mechanics of engineering fabrics using a mutually constrained pantographic beam and membrane mesh*. Composites Part A: Applied Science and Manufacturing, 2016. **81**: p. 145-157 DOI: 10.1016/j.compositesa.2015.11.005.
- [12] Dörr, D., F.J. Schirmaier, F. Henning, and L. Kärger, *A viscoelastic approach for modeling bending behavior in finite element forming simulation of continuously fiber reinforced composites*. Composites Part A: Applied Science and Manufacturing, 2017. **94**: p. 113-123 DOI: 10.1016/j.compositesa.2016.11.027.
- [13] Yu, F., S. Chen, J.V. Viisainen, M.P.F. Sutcliffe, L.T. Harper, and N.A. Warrior, *A macroscale finite element approach for simulating the bending behaviour of biaxial fabrics*. Composites Science and Technology, 2020. **191** DOI: 10.1016/j.compscitech.2020.108078.
- [14] Iwata, A., T. Inoue, N. Naouar, P. Boisse, and S.V. Lomov, *Coupled meso-macro simulation of woven fabric local deformation during draping*. Composites Part A: Applied Science and Manufacturing, 2019. **118**: p. 267-280 DOI: 10.1016/j.compositesa.2019.01.004.
- [15] Döbrich, O., T. Gereke, O. Diestel, S. Krzywinski, and C. Cherif, *Decoupling the bending behavior and the membrane properties of finite shell elements for a correct description of the mechanical behavior of textiles with a laminate formulation*. Journal of Industrial Textiles, 2013. **44**(1): p. 70-84 DOI: 10.1177/1528083713477442.
- [16] *British Standard. Textiles: test methods for nonwovens, in Part 7: Determination of bending length*. BS EN ISO 9073-7; 1998.
- [17] Boisse, P., J. Colmars, N. Hamila, N. Naouar, and Q. Steer, *Bending and wrinkling of composite fiber preforms and prepregs. A review and new developments in the draping simulations*. Composites Part B: Engineering, 2018. **141**: p. 234-249 DOI: 10.1016/j.compositesb.2017.12.061.
- [18] Harrison, P., M.F. Alvarez, and D. Anderson, *Towards comprehensive characterisation and modelling of the forming and wrinkling mechanics of engineering fabrics*. International Journal of Solids and Structures, 2017 DOI: 10.1016/j.ijstr.2016.11.008.
- [19] Lomov, S.V., I. Verpoest, M. Barburski, and J. Laperre, *Carbon composites based on multiaxial multiply stitched preforms. Part 2. KES-F characterisation of the deformability of the preforms*

- at low loads*. Composites Part A: Applied Science and Manufacturing, 2003. **34**(4): p. 359-370 DOI: 10.1016/s1359-835x(03)00025-3.
- [20] Potluri, P. and J. Atkinson, *Automated manufacture of composites: handling, measurement of properties and lay-up simulations*. Composites Part A: Applied Science and Manufacturing, 2003. **34**(6): p. 493-501 DOI: 10.1016/s1359-835x(03)00056-3.
- [21] Guzman-Maldonado, E., P. Wang, N. Hamila, and P. Boisse, *Experimental and numerical analysis of wrinkling during forming of multi-layered textile composites*. Composite Structures, 2019. **208**: p. 213-223 DOI: 10.1016/j.compstruct.2018.10.018.
- [22] Giorgio, I., P. Harrison, F. dell'Isola, J. Alsayednoor, and E. Turco, *Wrinkling in engineering fabrics: a comparison between two different comprehensive modelling approaches*. Proc Math Phys Eng Sci, 2018. **474**(2216): p. 20180063 DOI: 10.1098/rspa.2018.0063.
- [23] Arnold, S.E., M.P.F. Sutcliffe, and W.L.A. Oram, *Experimental measurement of wrinkle formation during draping of non-crimp fabric*. Composites Part A: Applied Science and Manufacturing, 2016. **82**: p. 159-169 DOI: 10.1016/j.compositesa.2015.12.011.
- [24] Shen, H., P. Wang, X. Legrand, and L. Liu, *Characterisation and optimisation of wrinkling during the forming of tufted three-dimensional composite preforms*. Composites Part A: Applied Science and Manufacturing, 2019. **127**: p. 105651 DOI: 10.1016/j.compositesa.2019.105651.
- [25] Andersson, A., *Evaluation and visualisation of surface defects on auto-body panels*. Journal of Materials Processing Technology, 2009. **209**(2): p. 821-837 DOI: 10.1016/j.jmatprotec.2008.02.078.
- [26] Dörr, D., T. Joppich, F. Schirmaier, T. Mosthaf, L. Kärgler, and F. Henning, *A method for validation of finite element forming simulation on basis of a pointwise comparison of distance and curvature*. 2016. **1769**: p. 170011 DOI: 10.1063/1.4963567.
- [27] Petitjean, S., *A survey of methods for recovering quadrics in triangle meshes*. ACM Computing Surveys, 2002. **34**(2): p. 211–262 DOI: doi:10.1145/508352.508354
- [28] Harrison, P., M.J. Clifford, and A.C. Long, *Shear characterisation of viscous woven textile composites: a comparison between picture frame and bias extension experiments*. Composites Science and Technology, 2004. **64**(10-11): p. 1453-1465 DOI: 10.1016/j.compscitech.2003.10.015.
- [29] Bouquerel, L., N. Moulin, S. Drapier, P. Boisse, and J.-M. Beraud, *Modelling and simulating the forming of new dry automated lay-up reinforcements for primary structures*. AIP Conference Proceedings, 2017. **1896**(1): p. 030008 DOI: 10.1063/1.5007995.
- [30] *CloudCompare 2.11*, Retrieved from, <http://www.cloudcompare.org>. Accessed
- [31] Badel, P., S. Gauthier, E. Vidal-Sallé, and P. Boisse, *Rate constitutive equations for computational analyses of textile composite reinforcement mechanical behaviour during forming*. Composites Part A: Applied Science and Manufacturing, 2009. **40**(8): p. 997-1007 DOI: 10.1016/j.compositesa.2008.04.015.
- [32] Chen, S., *Fabric forming simulation and process optimisation for composites*. 2016, University of Nottingham: Nottingham, UK.
- [33] Garimella, R.V. and B.K. Swartz, *Curvature Estimation for Unstructured Triangulations of Surfaces*. 2003, Los Alamos Nat. Lab.: Los Alamos.
- [34] Chen, S., A. Endruweit, L.T. Harper, and N.A. Warrior, *Inter-ply stitching optimisation of highly drapeable multi-ply preforms*. Composites Part A: Applied Science and Manufacturing, 2015. **71**: p. 144-156 DOI: 10.1016/j.compositesa.2015.01.016.
- [35] Krieger, H., T. Gries, and S.E. Stapleton, *Shear and drape behavior of non-crimp fabrics based on stitching geometry*. International Journal of Material Forming, 2017 DOI: 10.1007/s12289-017-1368-1.
- [36] Lin, H., J. Wang, A.C. Long, M.J. Clifford, and P. Harrison, *Predictive modelling for optimization of textile composite forming*. Composites Science and Technology, 2007. **67**(15-16): p. 3242-3252 DOI: 10.1016/j.compscitech.2007.03.040.

- [37] Chen, S., L.T. Harper, A. Endruweit, and N.A. Warrior, *Formability optimisation of fabric preforms by controlling material draw-in through in-plane constraints*. Composites Part A: Applied Science and Manufacturing, 2015. **76**: p. 10-19 DOI: 10.1016/j.compositesa.2015.05.006.

7 Tables

Table 1: Material parameters, including polynomial expressions for normalised shear force as a function of shear angle for two carbon fibre reinforcements. $M_{\text{nonlinear}}$ denotes the non-linear bending moment measured by the revised cantilever test; $B_{41.5^\circ}$ denotes the constant bending stiffness measured by the cantilever test at an angular deflection of 41.5° , according to BS EN ISO 9073-7 [16]. B_{init} is the bending stiffness at zero curvature and B_{inf} is the value taken from the asymptote of the non-linear bending curve as it approaches infinity.

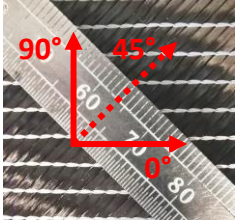
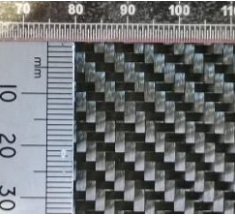
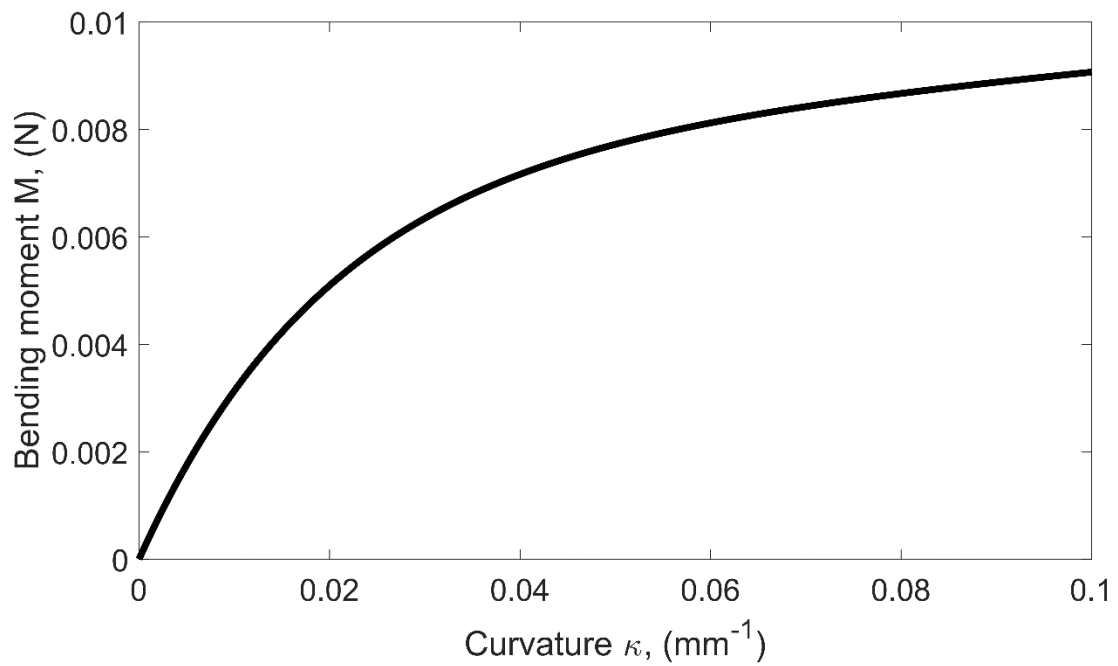
Materials	Parameters	Normalised shear curve	Bending property
Non-crimp fabric (NCF, FCIM359) 	Ply thickness 0.4 mm	$F_{\text{norm}}^{\text{NCF}} = F_{\text{norm}}^{\text{yarn rotation}} + F_{\text{norm}}^{\text{stitch}}$ [8] $F_{\text{norm}}^{\text{yarn rotation}} =$ $(29.56\gamma_{12}^5 - 65.56\gamma_{12}^4 + 137.06\gamma_{12}^3 + 94.73\gamma_{12}^2 + 112.19\gamma_{12}) \text{ N/m}$ $F_{\text{norm}}^{\text{stitch}} =$ $\begin{cases} (2000\gamma_{12} - 120) \text{ N/m}, & 0.06 \leq \gamma_{12} < 0.5 \\ (-3520\gamma_{12} + 2640) \text{ N/m}, & 0.5 \leq \gamma_{12} < 0.75 \\ 0 \text{ N/m}, & \text{else} \end{cases}$	Linear bending model (LBM) $B_{\text{init}}^{\text{NCF,pos}} = 0.0080 \text{ Nm}; B_{\text{init}}^{\text{NCF,neg}} = 0.0057 \text{ Nm}$ $B_{41.5^\circ}^{\text{NCF,pos}} = 0.0038 \text{ Nm}; B_{41.5^\circ}^{\text{NCF,neg}} = 0.0032 \text{ Nm}$ $B_{\text{inf}}^{\text{NCF,pos}} = 0.0002 \text{ Nm}; B_{\text{inf}}^{\text{NCF,neg}} = 0.0001 \text{ Nm}$
	Areal mass 440 gsm Fibre orientation $\pm 45^\circ$ Stitch orientation 0°		Non-linear bending model (NLBM) $M_{\text{nonlinear}}^{\text{NCF,pos}} = 0.19457 \cdot \kappa + 0.03139(1 - e^{(-\kappa/0.0040)}) \text{ N}$ $M_{\text{nonlinear}}^{\text{NCF,neg}} = 0.10279 \cdot \kappa + 0.03619(1 - e^{(-\kappa/0.0065)}) \text{ N}$
Woven fabric (38616) 	Ply thickness 0.3 mm	$F_{\text{norm}}^{\text{wov}} = 37.35\gamma_{12} - 322.61\gamma_{12}^2 + 1458.51\gamma_{12}^3 - 3539.56\gamma_{12}^4 +$ $4727.84\gamma_{12}^5 - 3275.20\gamma_{12}^6 + 930.53\gamma_{12}^7 \text{ N/m}$	Linear bending model (LBM) $B_{\text{init}}^{\text{wov}} = 0.00039 \text{ Nm}$ $B_{41.5^\circ}^{\text{wov}} = 0.00022 \text{ Nm}$ $B_{\text{inf}}^{\text{wov}} = 0.00002 \text{ Nm}$
	Areal mass 210 gsm Fibre orientation $0^\circ/90^\circ$		Non-linear bending model (NLBM) $M_{\text{nonlinear}}^{\text{wov}} = 0.01549 \cdot \kappa + 0.00757(1 - e^{(-\kappa/0.02)}) \text{ N}$

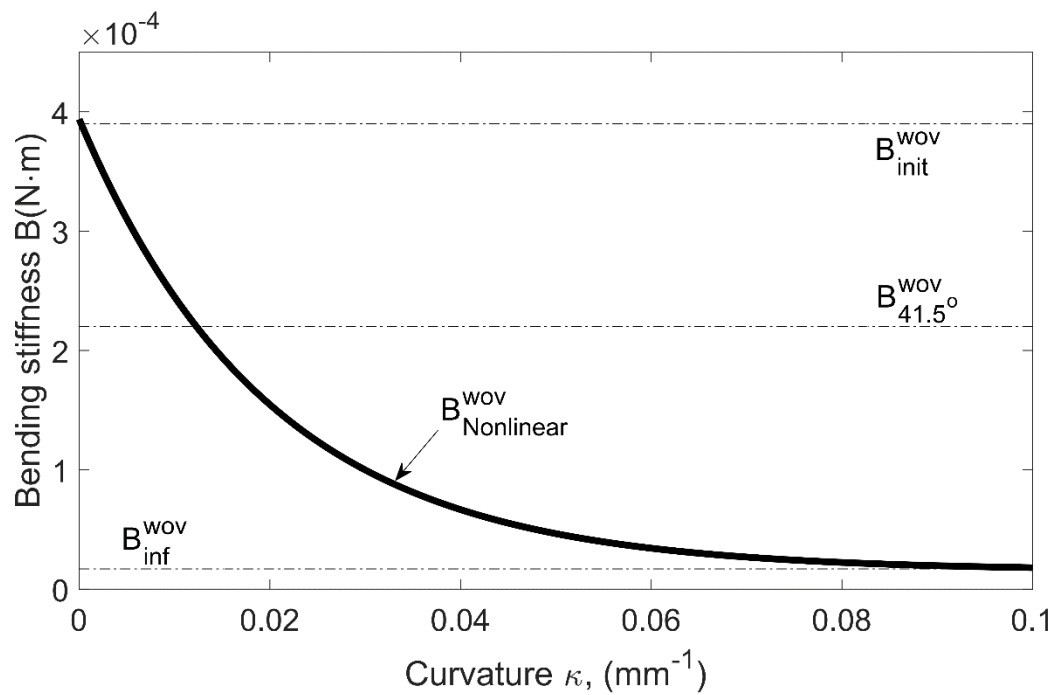
Table 2: Forming configuration, material, ply orientation and clamping method used for forming trials.

	Forming configuration	Material	Ply orientation	Clamping method
Case A		Woven fabric 38616	 [0/90]	Controlled gap (7 mm)
		NCF FCIM 359	 [+45/-45]	Controlled gap (7 mm)
Case B		NCF FCIM 359	 [+45/-45] ₂	Clamping force (1000 N)

8 Figures

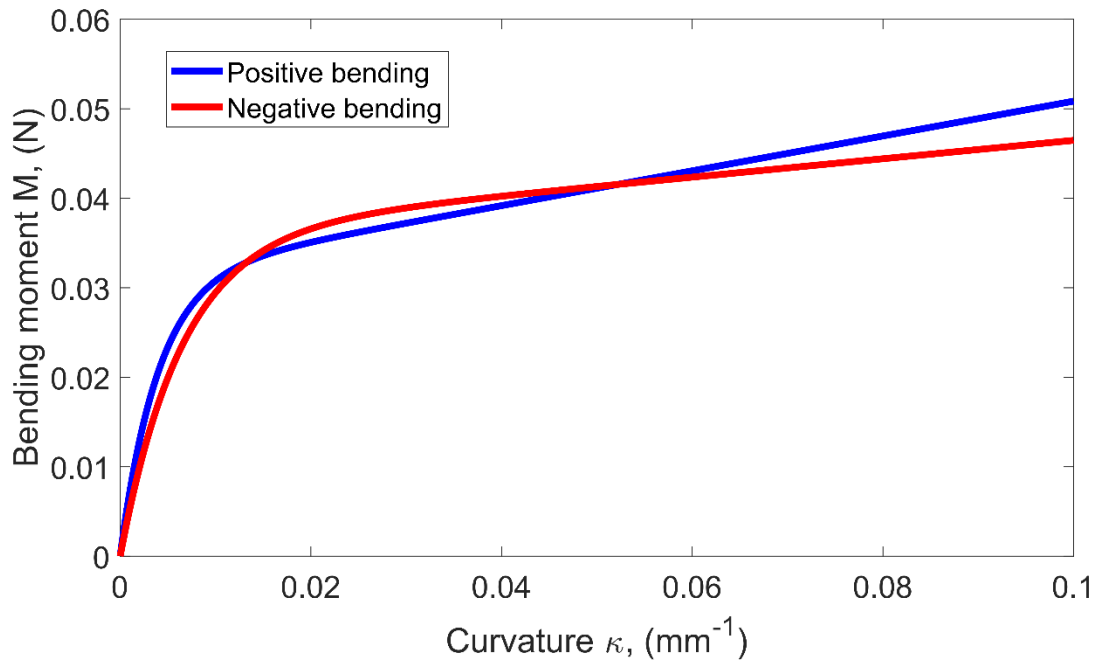


(a)

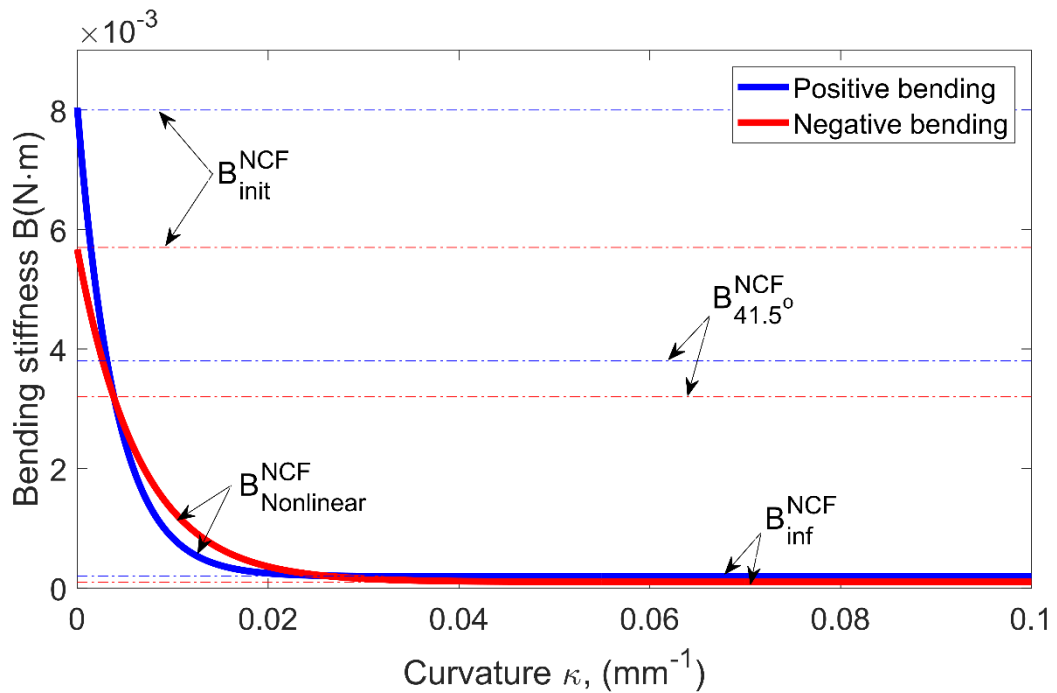


(b)

Figure 1: (a) Bending moment vs. curvature and (b) bending stiffness vs. curvature for the woven fabric ($B_{\text{Nonlinear}}$ denotes the non-linear bending stiffness measured by the revised cantilever test; $B_{41.5^\circ}$ denotes the constant bending stiffness measured by the standard cantilever test at an angular deflection of 41.5° according to BS EN ISO 9073-7 [16]).



(a)



(b)

Figure 2: (a) Bending moment vs. curvature and (b) bending stiffness vs. curvature relations for the NCF ($B_{\text{Nonlinear}}$ denotes the non-linear bending stiffness measured by the revised cantilever test; $B_{41.5^\circ}$ denotes the constant bending stiffness measured by the standard cantilever test at an angular deflection of 41.5° according to BS EN ISO 9073-7 [16]).

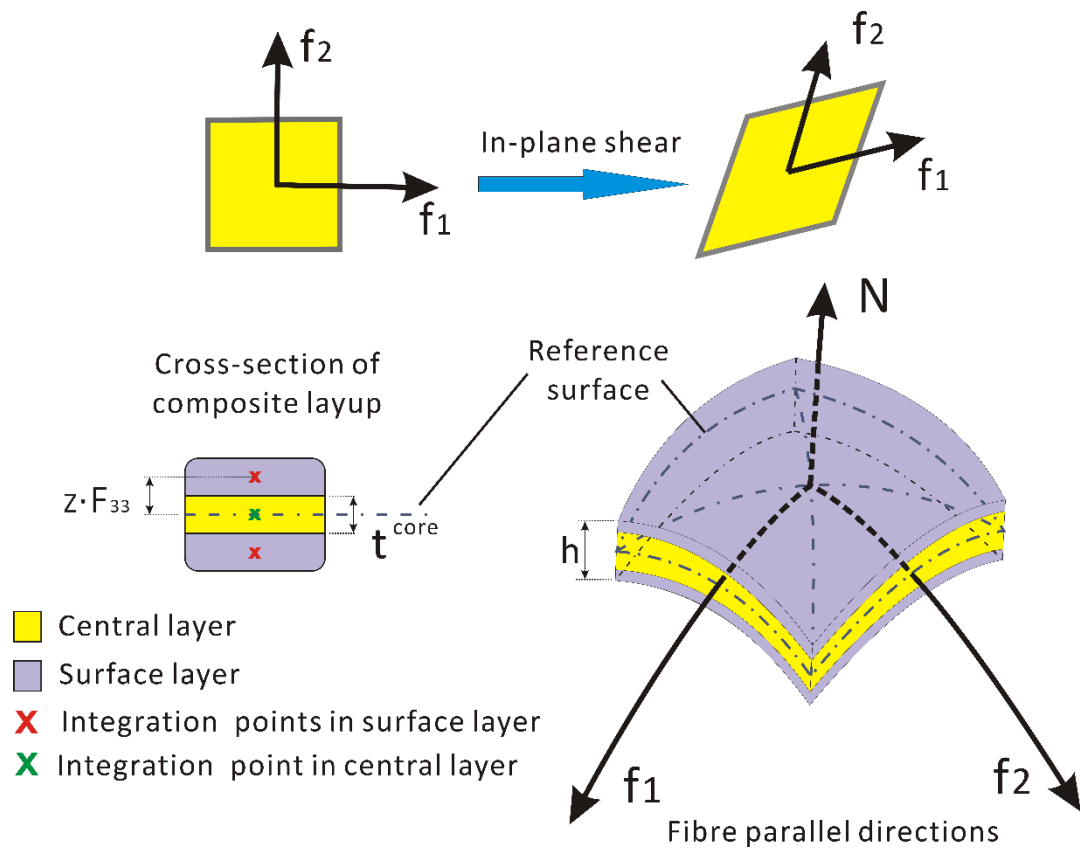


Figure 3: Schematic diagram of the shear deformation of a biaxial fabric unit cell and the laminate layup model for membrane/bending stiffness decoupling [13].

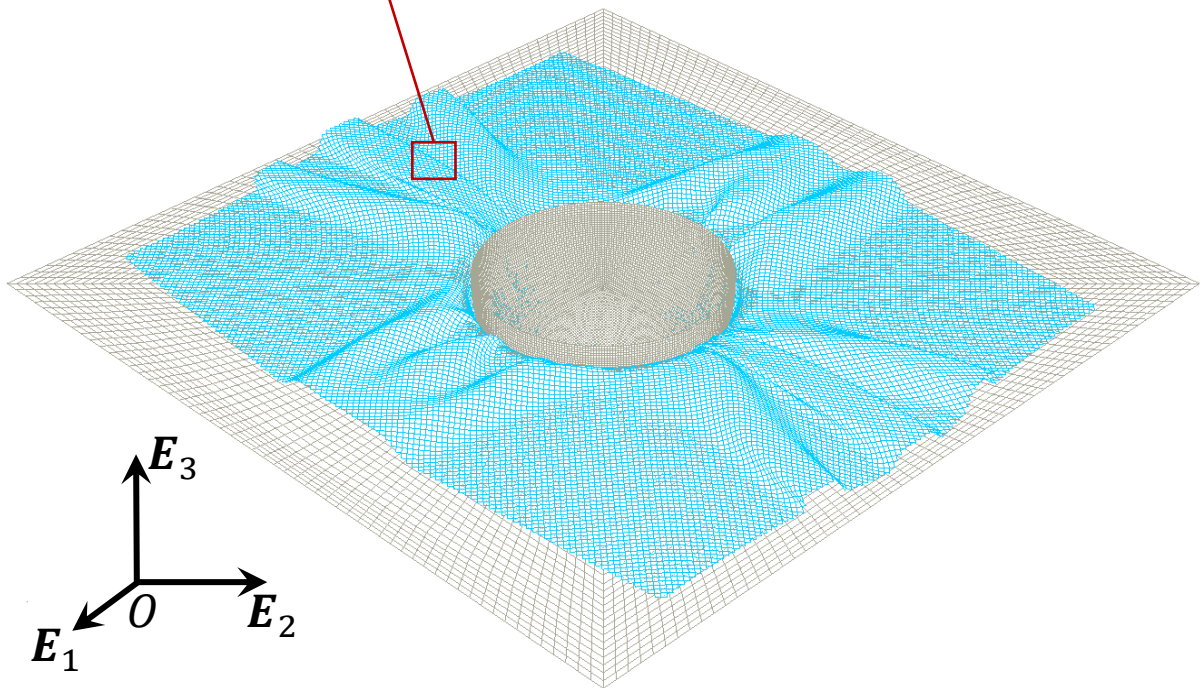
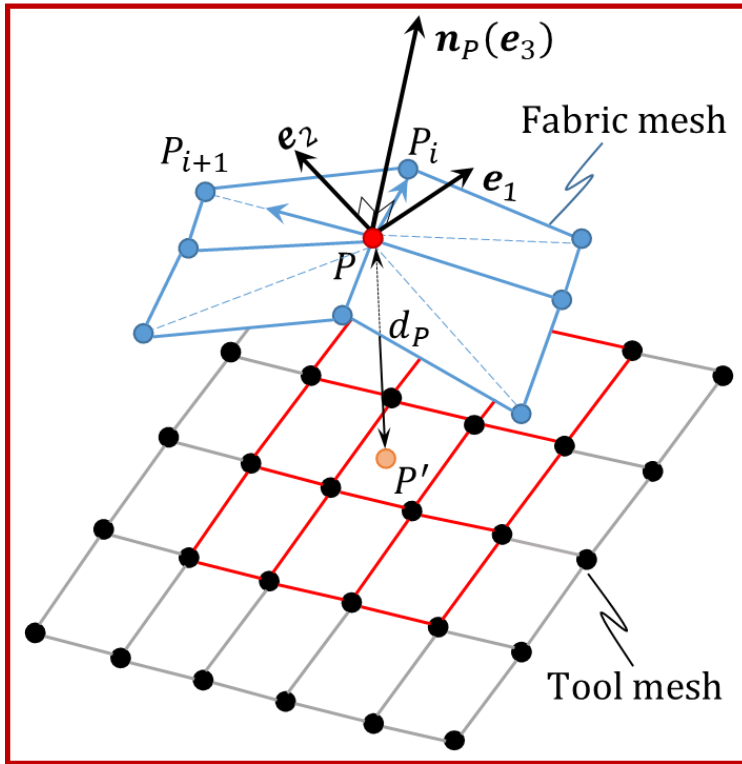


Figure 4: Schematic diagram to illustrate how the minimum nodal distance and nodal curvature is calculated between the fabric mesh and tool mesh

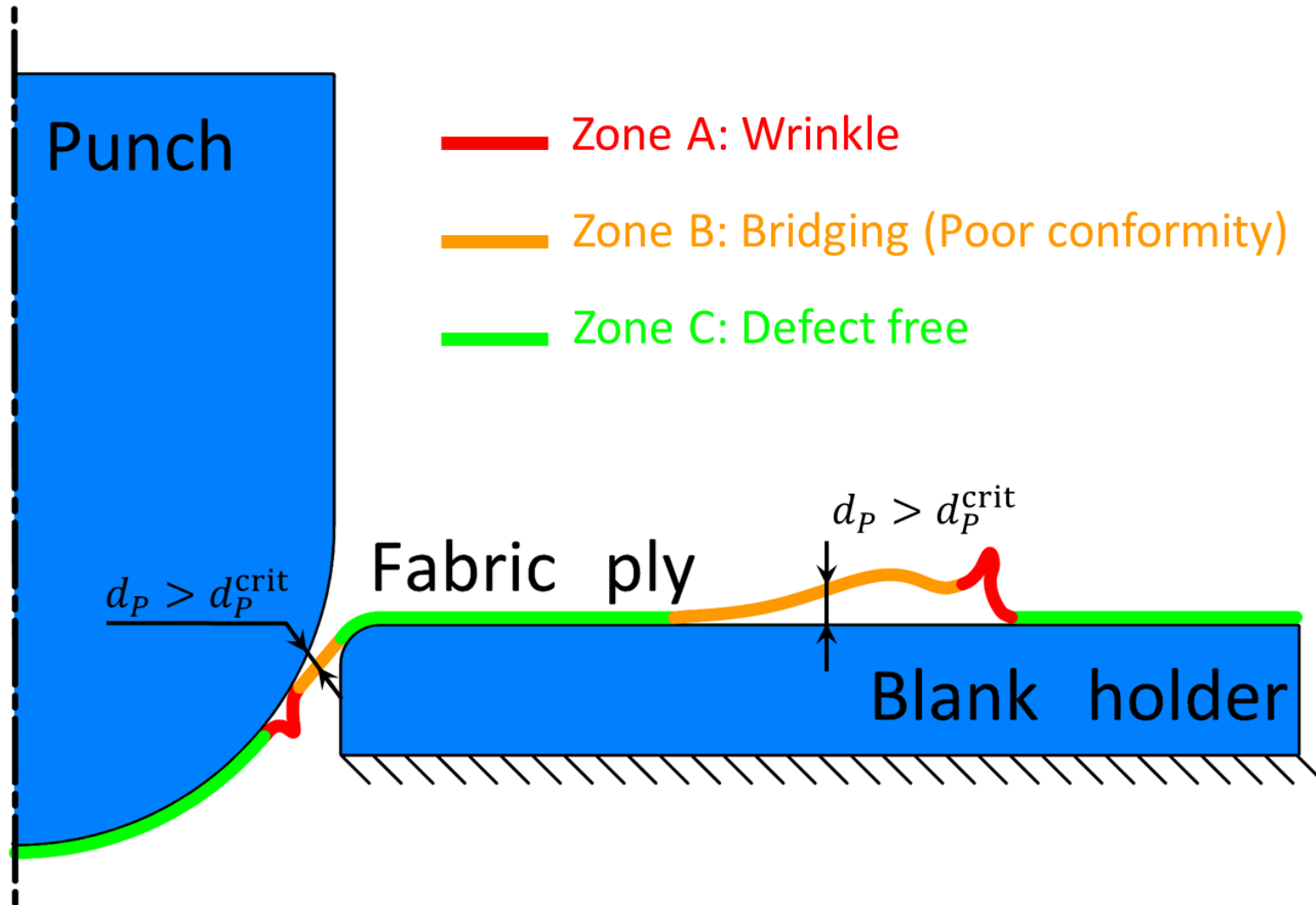


Figure 5: Schematic diagram to illustrate how surface defects are identified

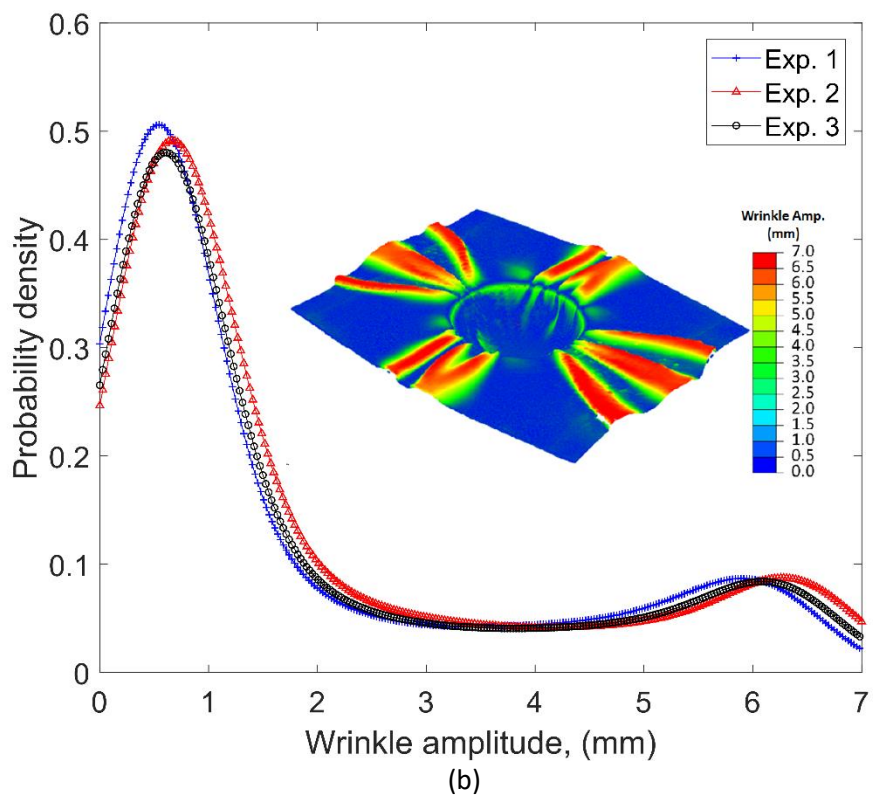
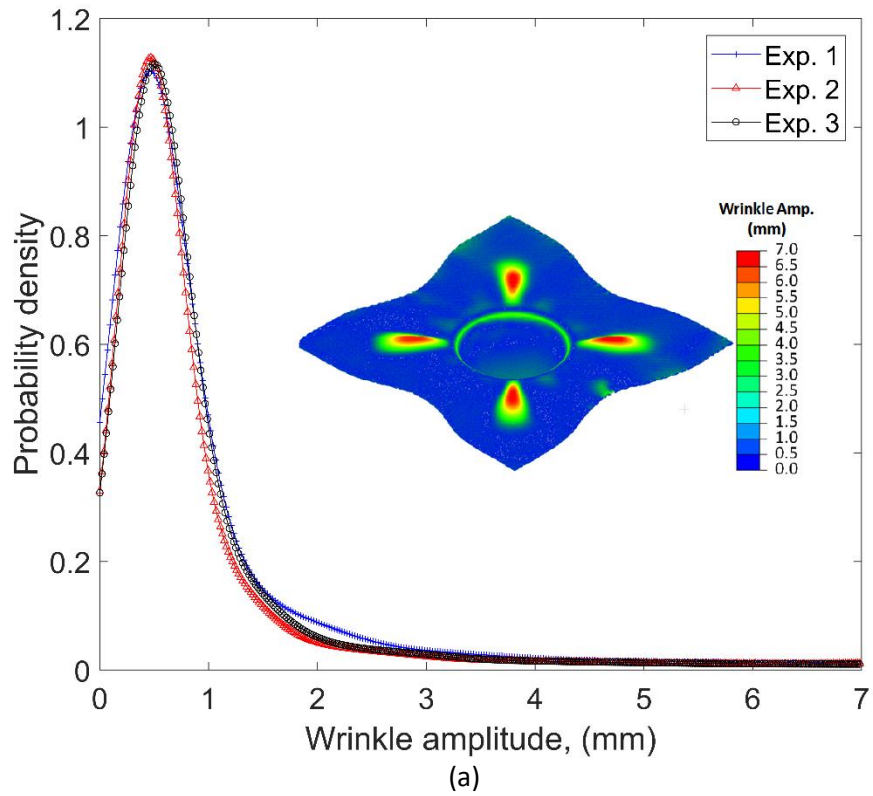


Figure 6: Probability density of wrinkle amplitude measured from three experimental repeats for the (a) woven fabric and (b) the NCF, for forming Case A. Inset images show examples of the experimental 3D scan data for each case, where the scale indicates wrinkle amplitude in millimetres.

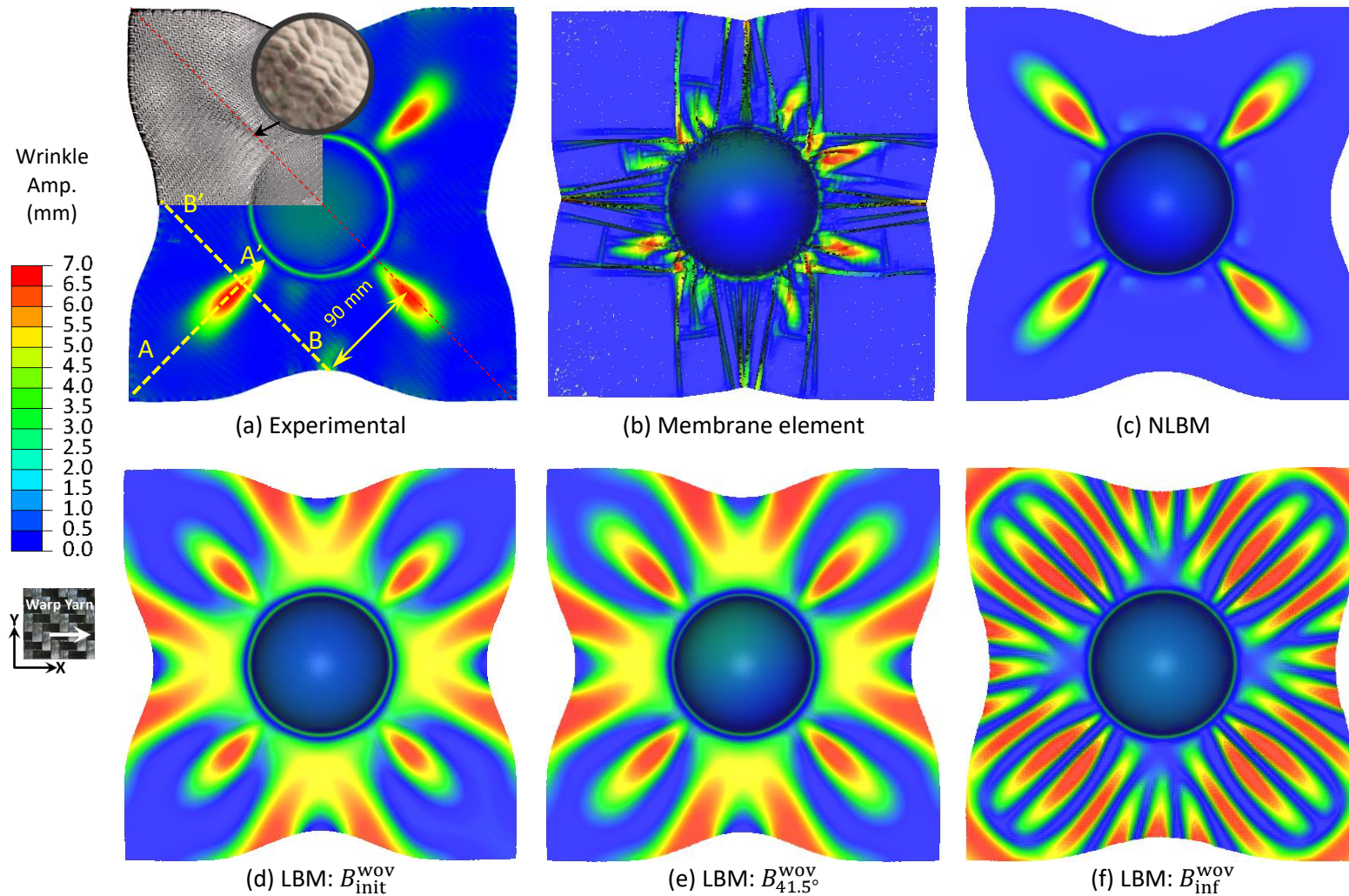


Figure 7: (a) Experimental wrinkle amplitude for the bi-axial woven fabric from forming Case A, measured by SWLS. Corresponding simulated wrinkle amplitudes using (b) membrane elements without bending stiffness, (c) non-linear bending model (NLBM), (d) linear bending model (LBM) using B_{init} , (e) LBM using the bending stiffness derived a constant angular deflection of 41.5° and (f) LBM using the asymptote stiffness value B_{inf} .

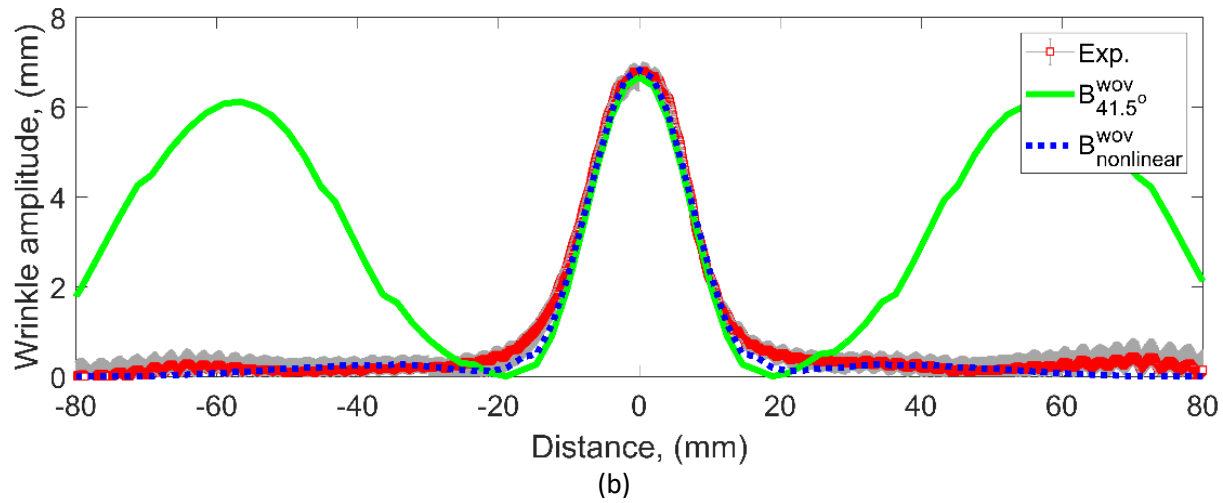
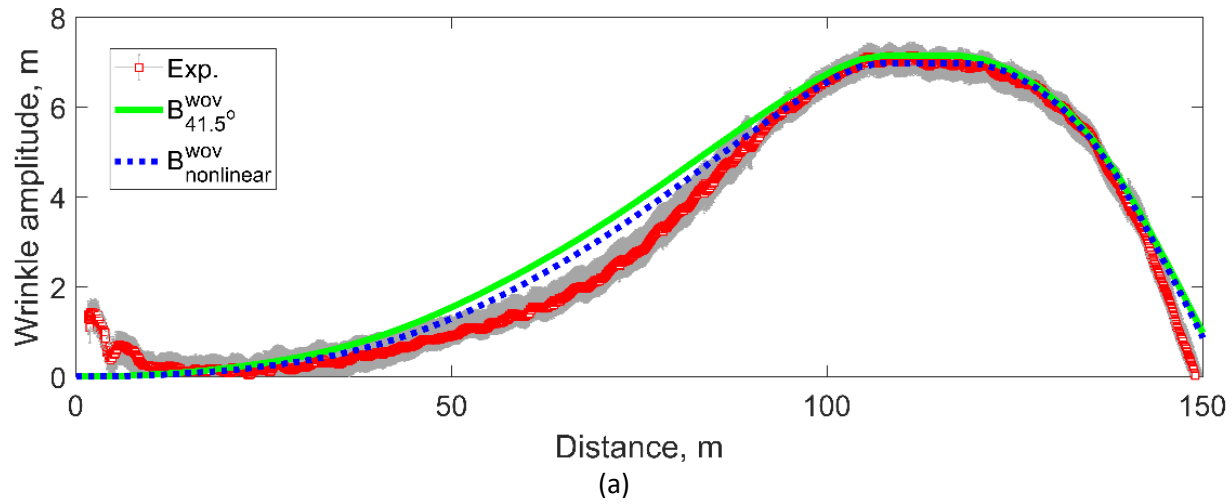


Figure 8: Wrinkle amplitudes for the woven material from forming Case A, predicted by the laminated shell element approach, using both linear and non-linear bending models along (a) path A-A' and (b) path B-B' (See Figure 7 for path definitions). Experimental data included for comparison.

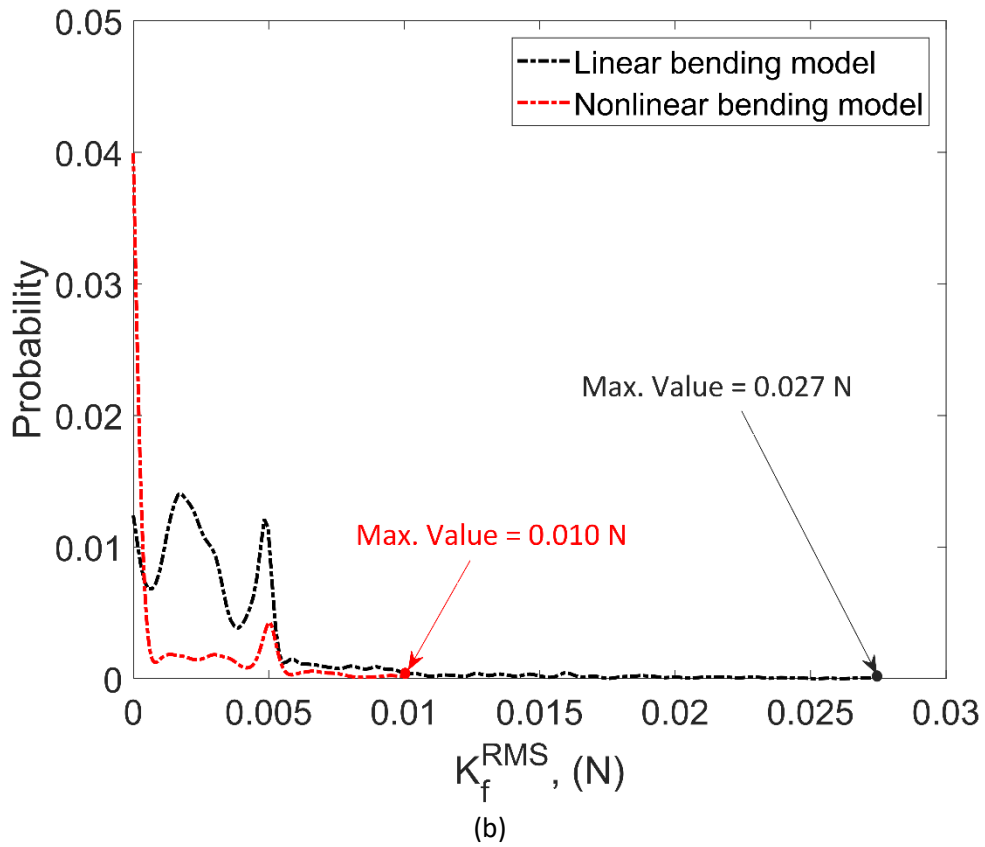
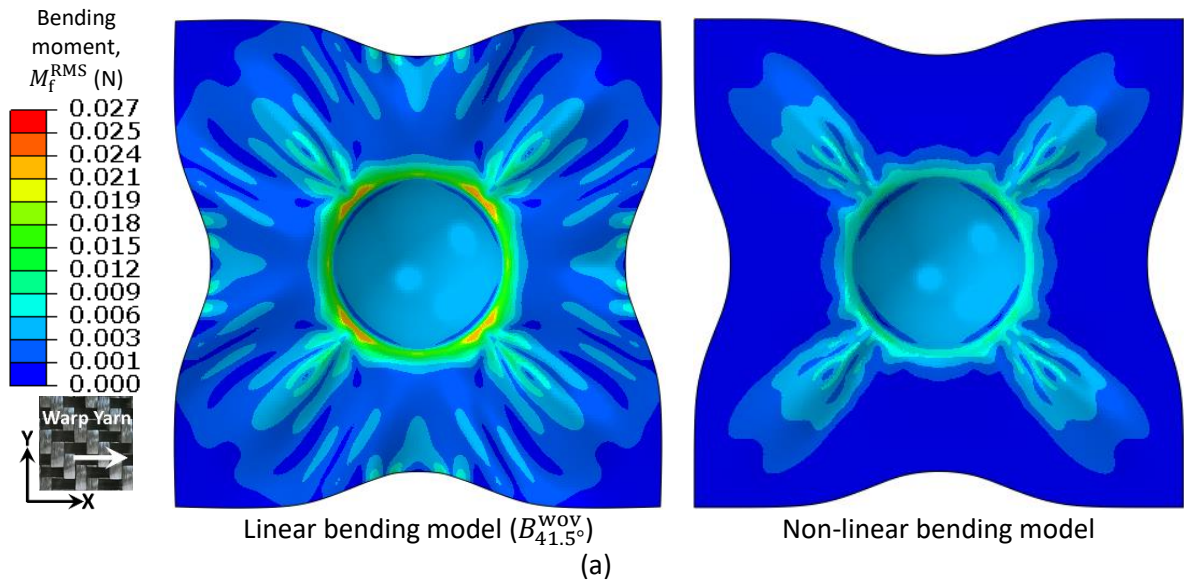


Figure 9: (a) The root mean square of the bending moments along the fibre directions, M_f^{RMS} and (b) the corresponding probability density function for the woven fabric from Case A, predicted by the linear and non-linear bending models.

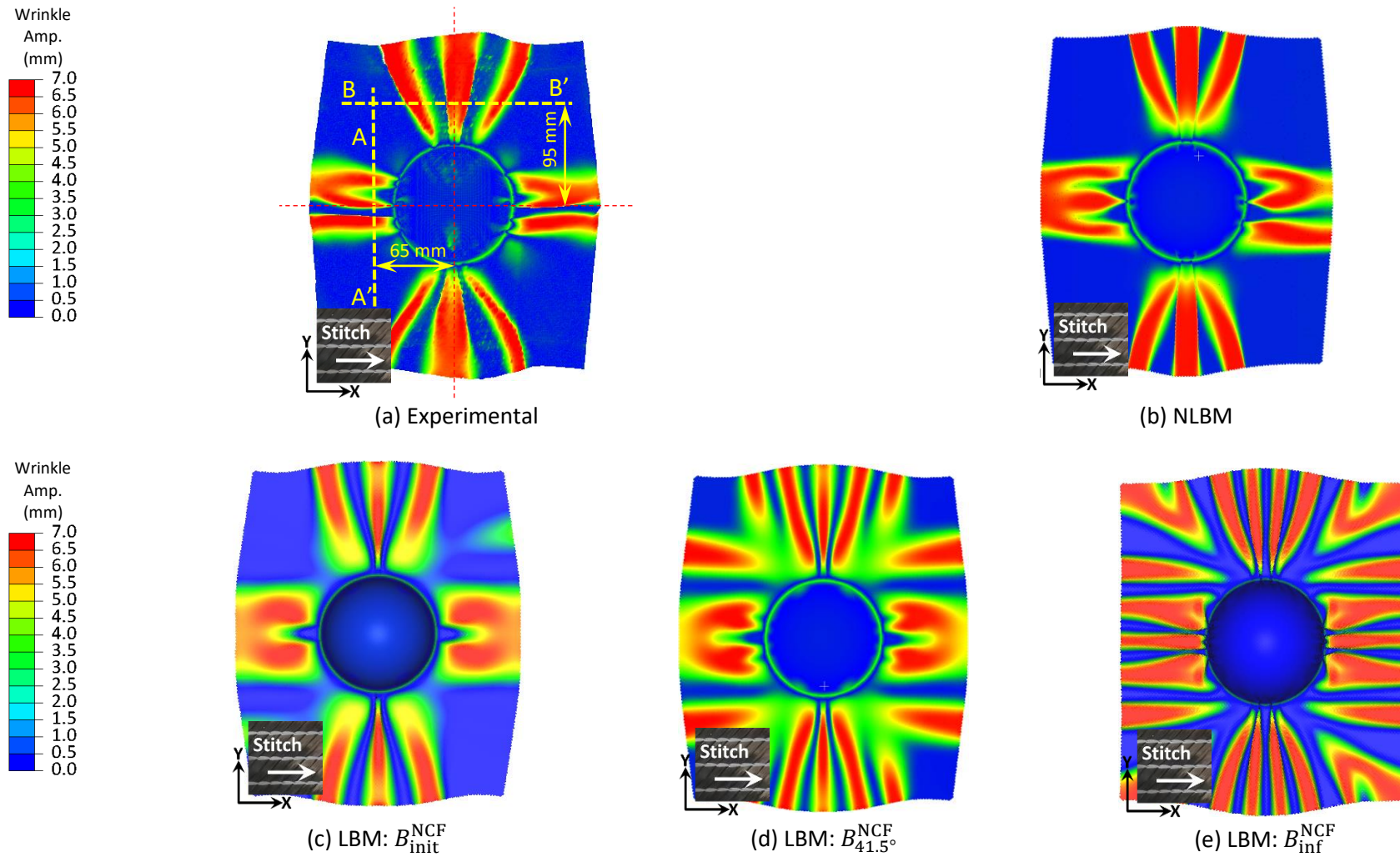
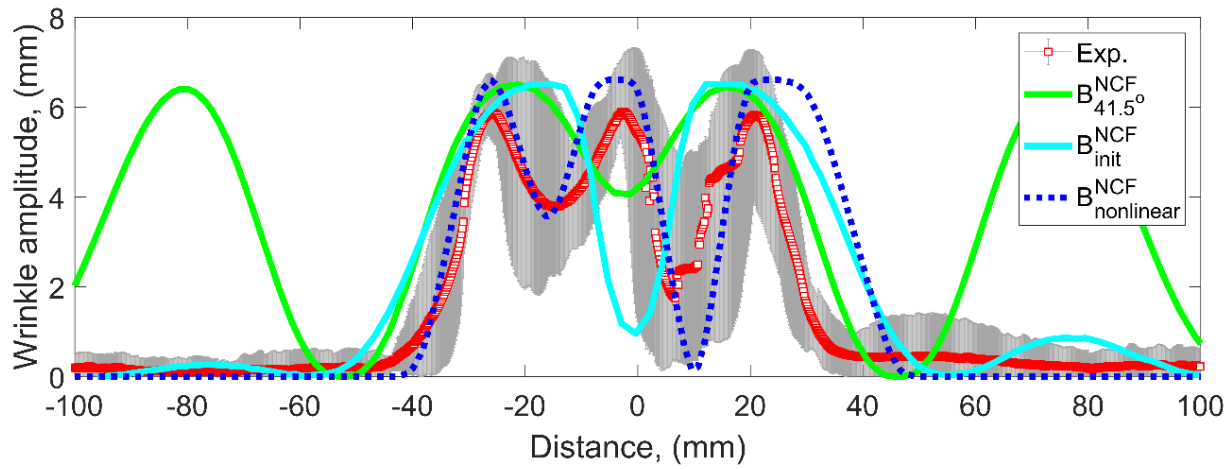
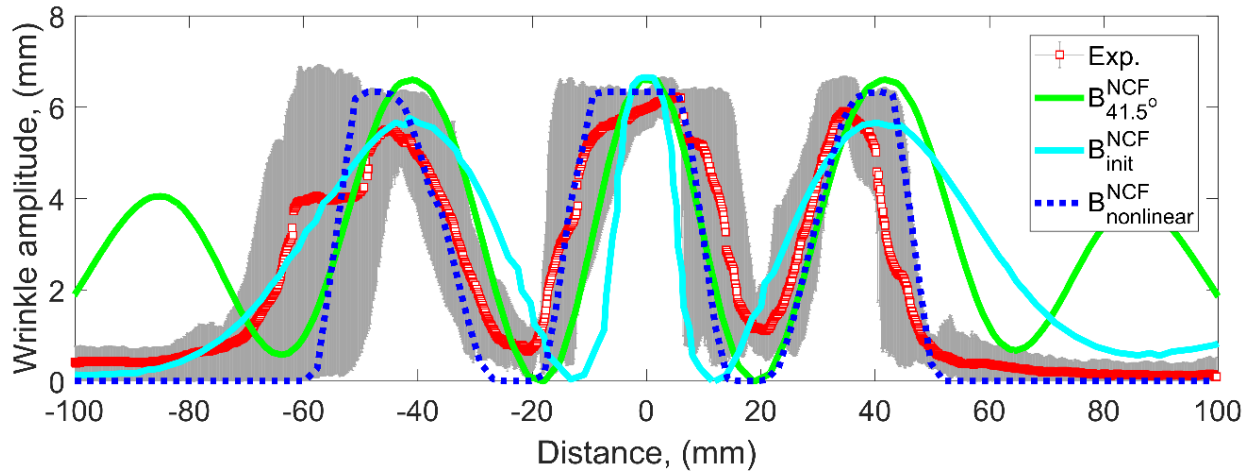


Figure 10: (a) Experimental wrinkle amplitude for the NCF from Case A measured by SWLS. Corresponding simulated wrinkle amplitudes using (b) Non-linear bending model (NLBM), (c) linear bending model (LBM) using B_{init} , (d) LBM using the bending stiffness derived from a constant angular deflection of 41.5° according to BS EN ISO 9073-7 [16] and (e) LBM using the asymptote stiffness value B_{inf} .



(a)



(b)

Figure 11: Wrinkle amplitudes for the NCF along paths (a) A-A' and (b) B-B' (see Figure 10(a) for path definitions) from Case A. Experimental data measured by SWLS, predictions produced by the linear (LBM) and non-linear bending models (NLBM).

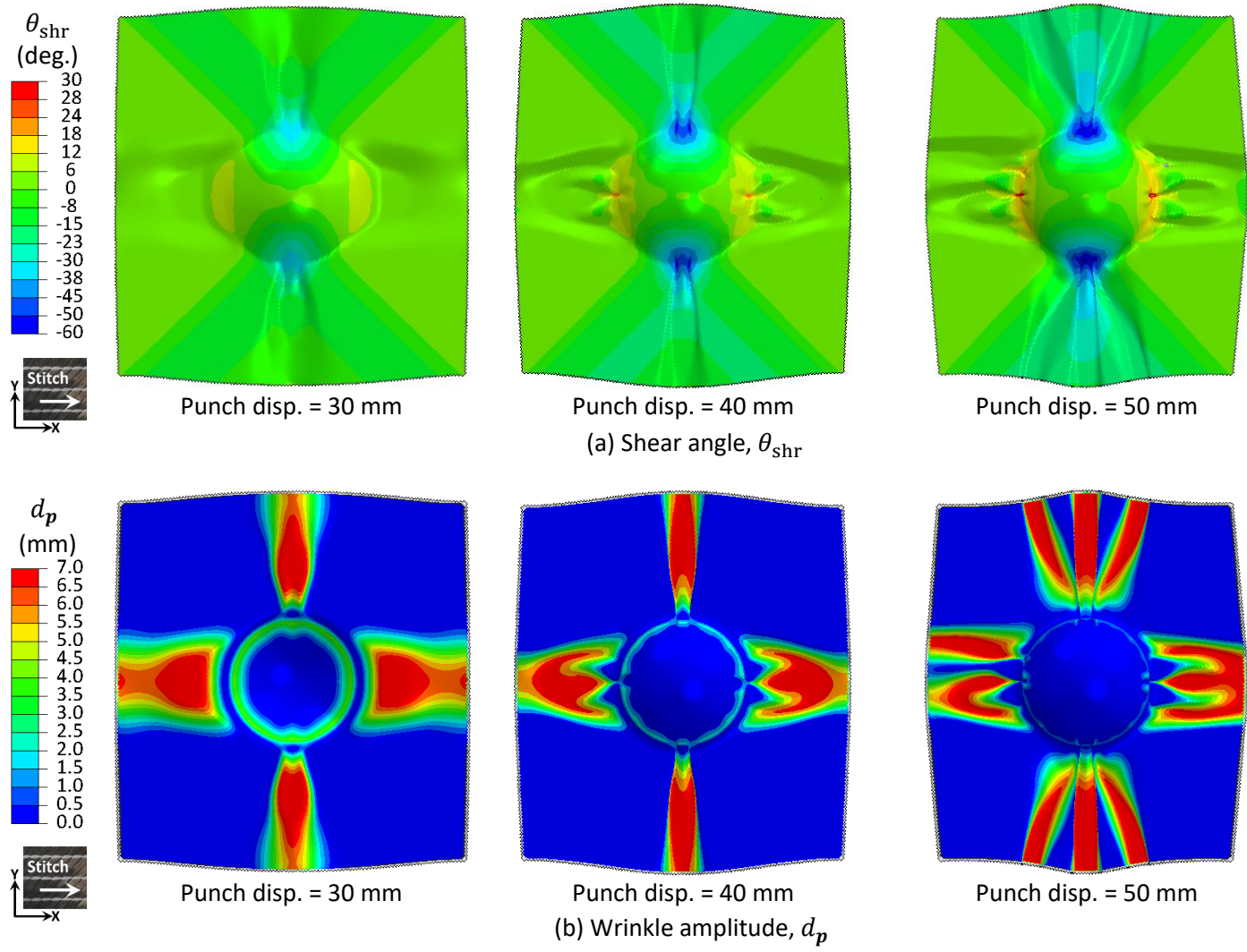


Figure 12: (a) Shear angle θ_{shr} and (b) wrinkle patterns according to the nodal deviation d_p at different punch displacements for the NCF material from Case A.

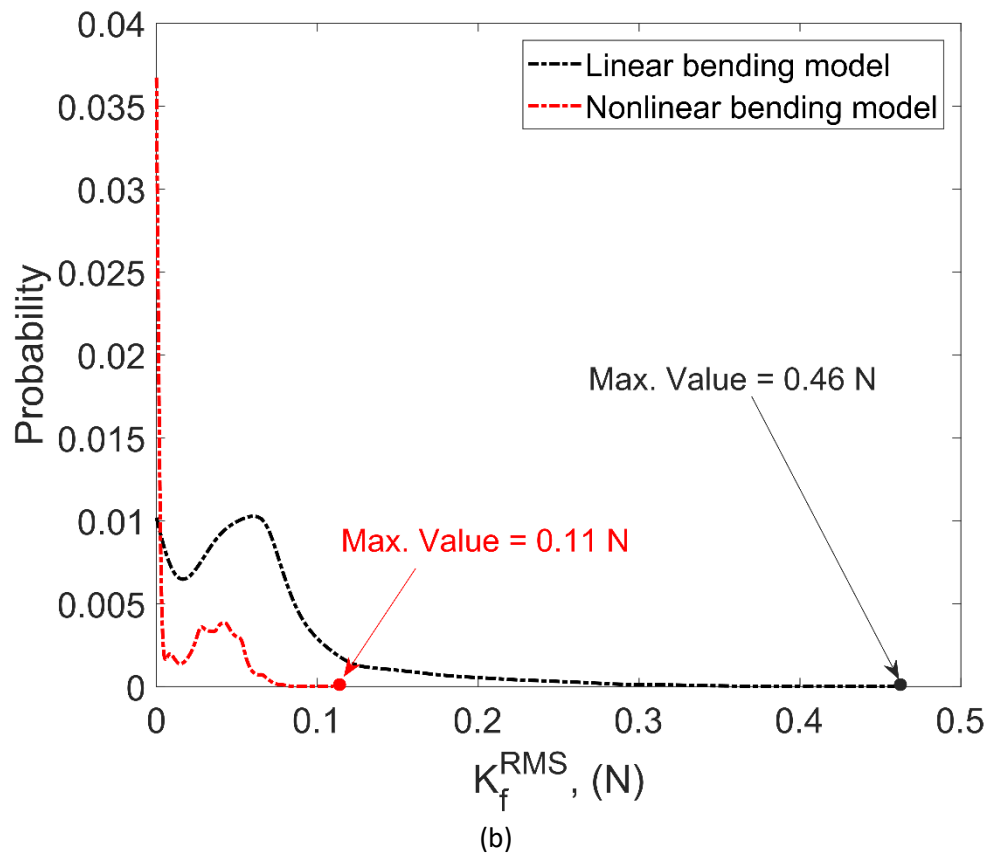
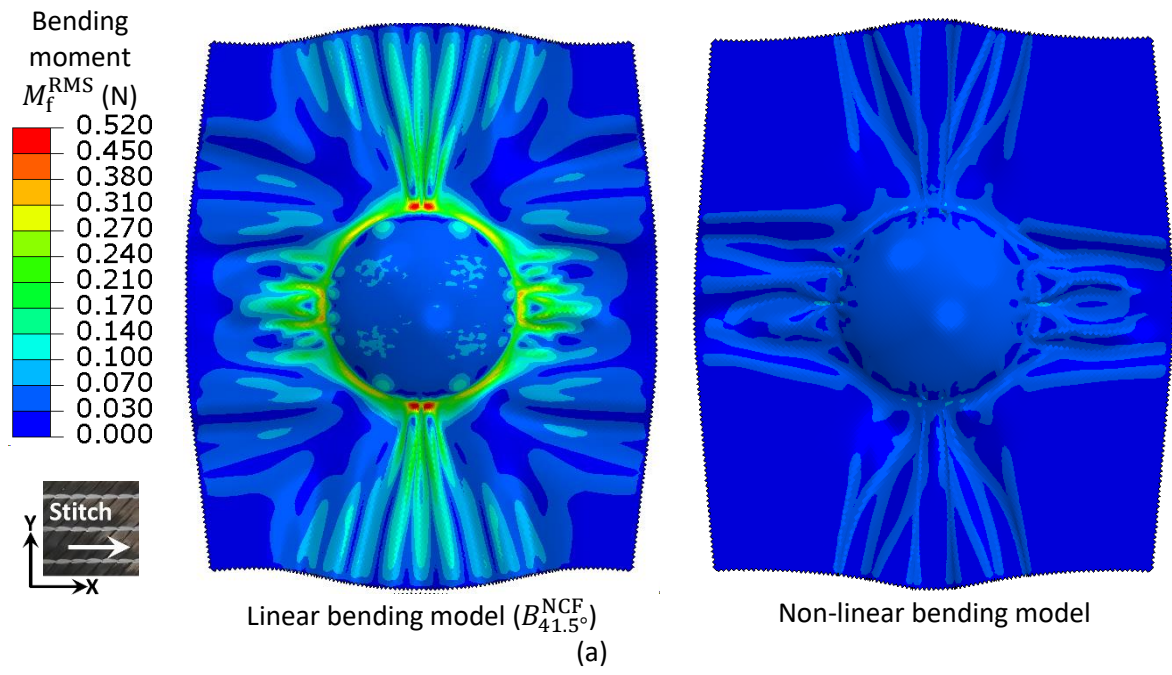


Figure 13: Bending moment along the warp yarn of the NCF from Case A, predicted by the linear and non-linear bending models

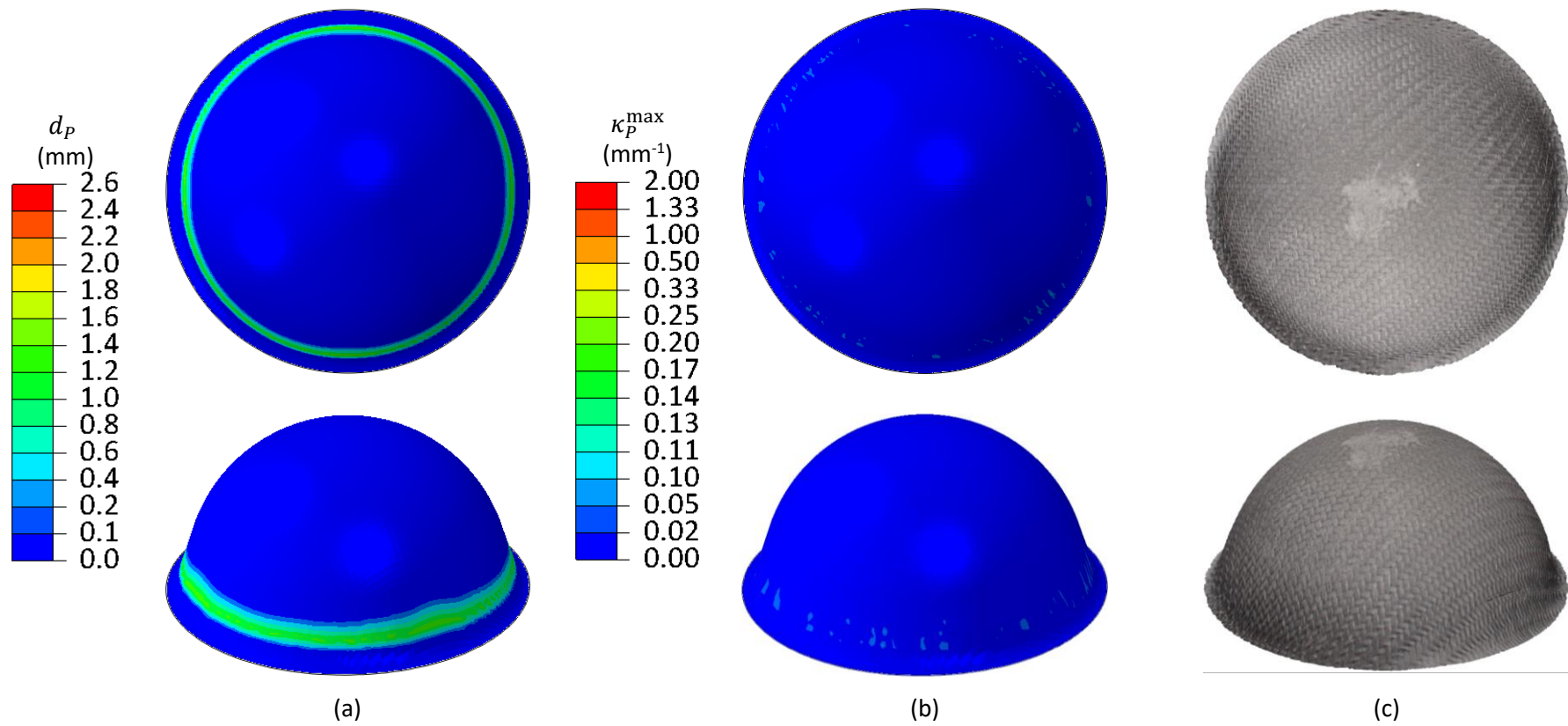
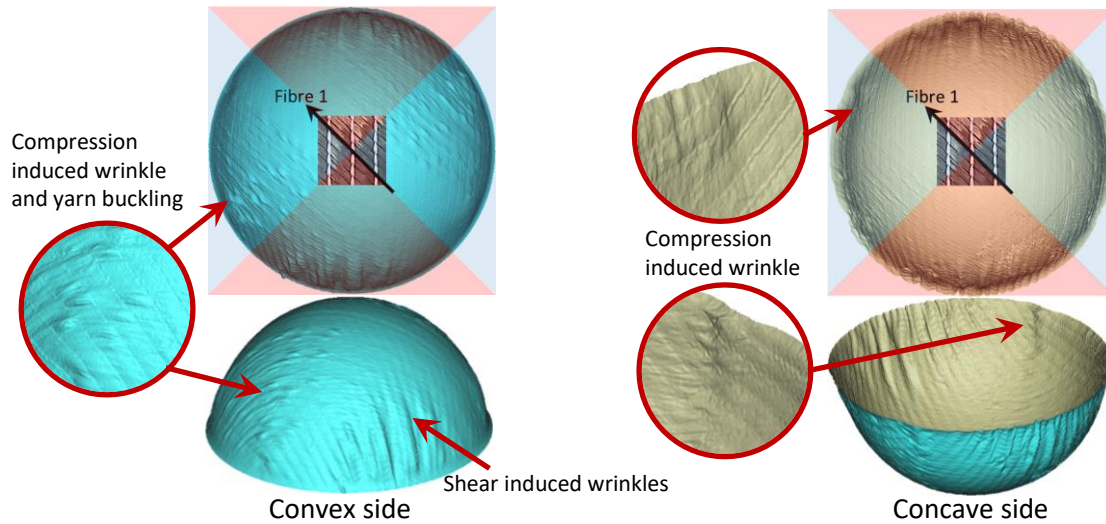


Figure 14: (a) predicted nodal deviation d_p and (b) surface curvature κ_p^{\max} for the woven fabric for forming Case B. (c) shows 3D scanned images from the SWLS.



(a)

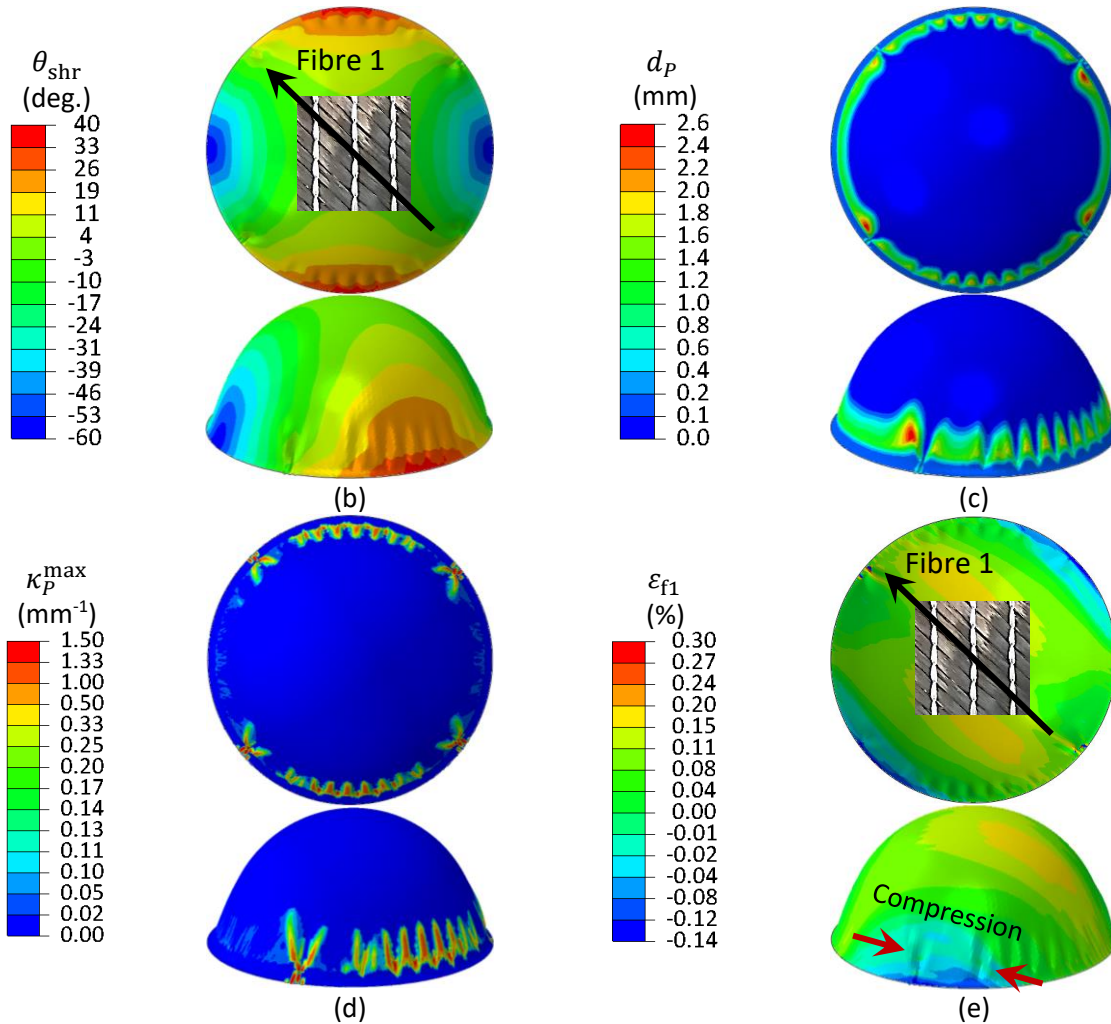


Figure 15: (a) Wrinkle shape captured by SWLS for both the concave and convex surfaces of the hemisphere. (b) Shear angle θ_{shr} , (c) predicted nodal deviation d_p , (d) surface curvature κ_p^{max} and (e) fibre strain along one fibre direction ϵ_{f1} for the NCF forming case B

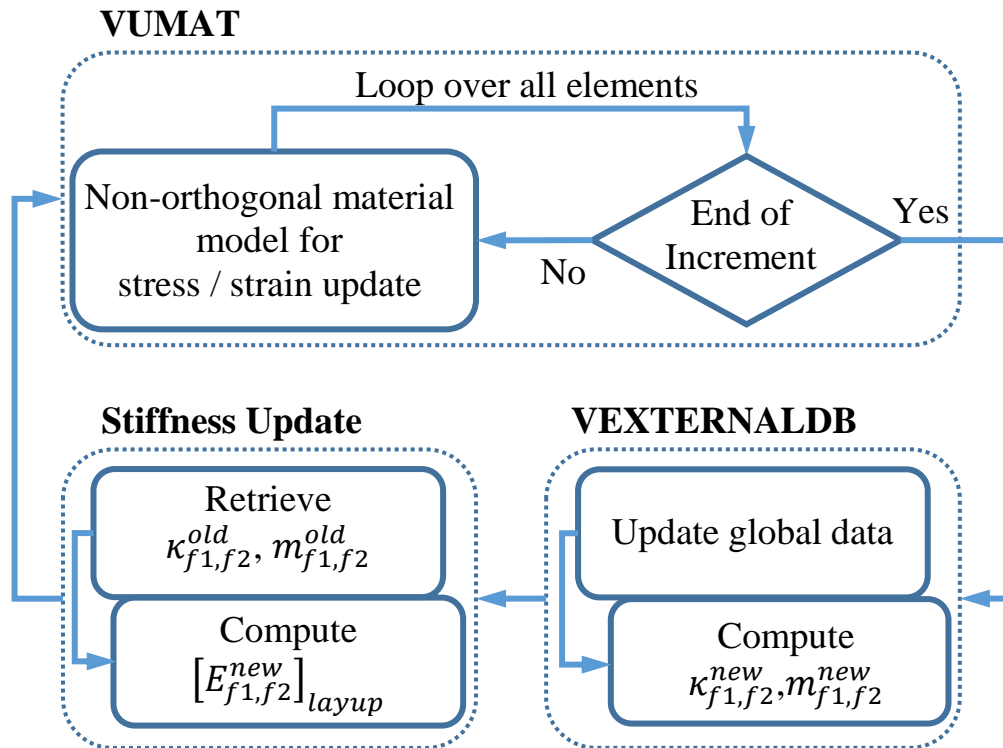


Figure A. 1: Flowchart for the implementation of the non-linear bending stiffness into the Abaqus VUMAT to update the bending moment and curvature. Superscripts “old” and “new” denote quantities at the beginning and the end of each increment, respectively.